Article

Immunity

Protective human monoclonal antibodies target conserved sites of vulnerability on the underside of influenza virus neuraminidase

Graphical abstract

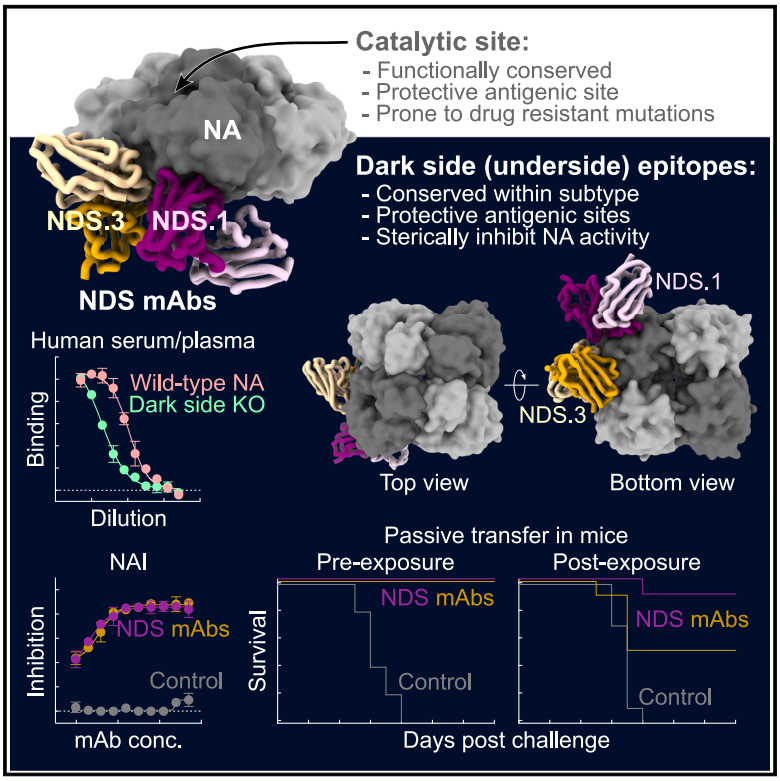

Highlights

- Isolation of broadly cross-reactive and protective N2 NA-targeting human antibodies
- Cryo-EM structures of two broadly cross-reactive antibodies in complex with N2 NA
- Identification of conserved non-overlapping epitopes on the underside of NA head
- Detection of antibodies to the NA underside epitopes in human convalescent samples

Authors

Julia Lederhofer, Yaroslav Tsybovsky, Lam Nguyen, ..., Sarah F. Andrews, Neil P. King, Masaru Kanekiyo

Correspondence

kanekiyom@nih.gov

In brief

Influenza neuraminidase (NA) is underappreciated as a vaccine target owing to its incomplete epitope landscape. Lederhofer et al. isolated human monoclonal antibodies to NA underside (i.e., dark side) epitopes with broad cross-reactivity across N2 subtype and protective efficacy in pre- and post-exposure settings, providing insights for NA-based vaccine design.

Lederhofer et al., 2024, Immunity *57*, 574–586
March 12, 2024 Published by Elsevier Inc.
https://doi.org/10.1016/j.immuni.2024.02.003

CellPress

CellPress
OPEN ACCESS

Immunity

Article

Protective human monoclonal antibodies target conserved sites of vulnerability on the underside of influenza virus neuraminidase

Julia Lederhofer,[1] Yaroslav Tsybovsky,[2] Lam Nguyen,[1] Julie E. Raab,[1] Adrian Creanga,[1] Tyler Stephens,[2] Rebecca A. Gillespie,[1] Hubza Z. Syeda,[1] Brian E. Fisher,[1] Michelle Skertic,[1] Christina Yap,[1] Andrew J. Schaub,[1] Reda Rawi,[1] Peter D. Kwong,[1] Barney S. Graham,[1,5] Adrian B. McDermott,[1,6] Sarah F. Andrews,[1] Neil P. King,[3,4] and Masaru Kanekiyo[1,7,*]

[1]Vaccine Research Center, National Institute of Allergy and Infectious Diseases, National Institutes of Health, Bethesda, MD 20892, USA
[2]Vaccine Research Center Electron Microscopy Unit, Cancer Research Technology Program, Frederick National Laboratory for Cancer Research sponsored by the National Cancer Institute, Frederick, MD 21702, USA
[3]Department of Biochemistry, University of Washington, Seattle, WA 98195, USA
[4]Institute for Protein Design, University of Washington, Seattle, WA 98195, USA
[5]Present address: Morehouse School of Medicine, Atlanta, GA 30310, USA
[6]Present address: Sanofi, Lyon 69007, France
[7]Lead contact
*Correspondence: kanekiyom@nih.gov
https://doi.org/10.1016/j.immuni.2024.02.003

SUMMARY

Continuously evolving influenza viruses cause seasonal epidemics and pose global pandemic threats. Although viral neuraminidase (NA) is an effective drug and vaccine target, our understanding of the NA antigenic landscape still remains incomplete. Here, we describe NA-specific human antibodies that target the underside of the NA globular head domain, inhibit viral propagation of a wide range of human H3N2, swine-origin variant H3N2, and H2N2 viruses, and confer both pre- and post-exposure protection against lethal H3N2 infection in mice. Cryo-EM structures of two such antibodies in complex with NA reveal non-overlapping epitopes covering the underside of the NA head. These sites are highly conserved among N2 NAs yet inaccessible unless the NA head tilts or dissociates. Our findings help guide the development of effective countermeasures against ever-changing influenza viruses by identifying hidden conserved sites of vulnerability on the NA underside.

INTRODUCTION

Circulating seasonal influenza viruses cause substantial morbidity and mortality and pose global public health and economic challenges.[1,2] In addition, a new influenza pandemic on the scale last seen in 1918 could potentially claim tens or hundreds of millions of lives worldwide.[3] Current influenza vaccines mainly induce antibodies against the surface glycoprotein hemagglutinin (HA) that can block viral attachment to its host receptors and/or viral membrane fusion to the host cell.[4] These antibodies primarily target the immunodominant head region of HA, which undergoes antigenic drift in response to immune pressure.[5] As a result, vaccine-elicited antibodies provide protection against vaccine-matched strains of the virus, but they confer little cross-protection from other strains or subtypes. Considerable effort in influenza vaccine design has been directed at developing immunogens that elicit broadly neutralizing antibody responses to subdominant epitopes of HA, like the HA stem domain, and discovery of new broadly conserved viral sites of vulnerability remains a priority for next-generation influenza vaccine development.[6–9]

Neuraminidase (NA) is a less abundant but essential surface protein of influenza viruses.[10] NA cleaves sialic acid from glycoproteins and glycolipids on the host cell surface, allowing progeny viruses to be released from infected cells.[11] In addition, NA is suggested to play a role in facilitating virion navigation through the respiratory tract by cleaving off decoy receptors present in the mucus and mucosal membranes.[12] The catalytic activity of NA is one of the main targets of influenza antivirals, and NA inhibitors have been widely utilized to treat influenza in humans for more than two decades. NA has re-emerged as a vaccine target due to the discovery of a number of human anti-NA antibodies that can inhibit NA activity by directly targeting or sterically blocking its catalytic site.[4,13–15] Although hemagglutination inhibition (HAI) has long been considered the main correlate of protection, it is now appreciated that both NA inhibition (NAI) and NA-binding antibodies also correlate with protection and reduced viral shedding.[12,16–20]

Two human broadly cross-reactive anti-NA monoclonal antibodies (mAbs), 1G01 and DA03E17, have been described.[14,15] 1G01 was isolated from an H3N2-infected individual shortly after the onset of symptoms. This antibody targets the catalytic site of NA with an extended complementarity-determining region H3 loop (CDR H3) and inhibits virtually all NA subtypes of influenza A and B viruses *in vivo* and *in vitro*. DA03E17, isolated using the hybridoma method from an individual who was infected with A(H1N1)pdm09 virus, binds to or near the enzymatic active site and shows similarly broad protection *in vivo* and *in vitro*. Another group discovered two influenza B anti-NA mAbs that broadly protect against both Yamagata- and Victoria-lineage viruses by targeting the catalytic site of NA.[13] Furthermore, the murine mAb CD6 protects against A(H1N1)pdm09 by binding to an epitope on the "side" of the NA globular head domain that spans two neighboring protomers and inhibits the catalytic activity of NA through steric hindrance.[21] Similar mAbs have been isolated from an individual upon natural H7N9 influenza infection[22,23] and a mouse infected with H1N8 virus.[24]

Given the fact that the murine mAb CD6 was induced by infection and its almost perpendicular angle of approach to the NA head, it is plausible that the NA head may be flexible on the viral surface. Casalino et al. describe the dynamics of influenza glycoproteins in a crowded protein environment using mesoscale all-atom molecular dynamics simulations, and they revealed that the NA globular head domain can tilt up to 90° on the virion, exposing the lateral as well as the "underside" surface of NA globular head to immune recognition.[25] High-resolution cryoelectron tomography (cryo-ET) indicates similar tilting by the SARS-CoV-2 spike protein on the surface of virions[26] and by influenza HA on a detergent micelle.[27] Furthermore, structural studies of viral glycoproteins with similar three-dimensional folds as influenza NA, notably Nipah G, have revealed dissociation of the four head domains and antibody binding to the underside of the head.[28] Combined with longstanding observations that recombinant NA proteins have a tendency to dissociate,[22,23,29] these studies suggest that additional epitopes on NA may be targeted by biologically relevant antibodies. Therefore, characterization of such antibodies and their epitopes can help aid the design of NA-based antigens for next-generation influenza vaccines.[30,31]

In this study, we isolated human NA-specific mAbs from two human individuals with H3N2 virus infection and found that several of them target conserved epitopes on the underside of the globular head of N2 NAs. These mAbs inhibit H3N2 and H2N2 virus propagation *in vitro* and confer protection against H3N2 infection in mice in both prophylactic and therapeutic settings. Cryoelectron microscopy (cryo-EM) structures of two such mAbs in complex with N2 NA defined in atomic detail the epitopes on the NA "dark side" (NDS), a forgotten antigenic site originally suggested nearly 40 years ago.[32]

RESULTS

Isolation of broadly cross-reactive N2 NA-targeting antibodies from two human convalescent donors

To characterize NA-directed B cell responses upon H3N2 virus infection in humans, peripheral blood mononuclear cells (PBMCs) were collected from two convalescent individuals who had a confirmed influenza A H3N2 infection in 2015 and 2021 ("donor A" and "donor B," respectively). Antigen-specific B cells were single-cell sorted from PBMCs with N2 NA probes (Figure S1) and corresponding heavy- and light-chain variable genes were sequenced. We recovered a total of 44 and 66 paired immunoglobulin heavy- and light-chain gene sequences from donor A and donor B, respectively, and analyzed their immunogenetic composition (Figure 1A). We found that there were several clonal expansions of NA-specific immunoglobulin sequences in donor A samples, likely associated with the recent H3N2 infection, whereas donor B had mostly unique sequences with only a few expanded clones. Representative immunoglobulin heavy- and light-chain genes were subcloned into human IgG1 backbone vectors, and recombinant mAbs were produced in mammalian cells by transient transfection of corresponding heavy- and light-chain plasmids. Among 16 mAbs from donor A and 20 mAbs from donor B, which we cloned, we identified six mAbs (NDS.1, NDS.1.1, NDS.1.2, and NDS.3 from donor A; and NDS.5 and NDS.6 from donor B) that bind to all four members of a panel of four N2 NAs from three seasonal H3N2 viruses and one swine-origin variant H3N2 (H3N2v) virus (Figure 1B). Immunoglobulin genes of these antibodies were between 5.8% and 10.5% divergent from their inferred germline V_H genes and between 3.2% and 7.9% divergent from their inferred germline V_K/V_L genes (Table S1). Overall, these mAbs bound equally well to the four tested N2 NAs with the exception of NDS.6, which showed lower binding to two out of four NAs. When we compared our mAbs to 1G01, the most well-characterized NA catalytic site-directed mAb,[15] our mAbs exhibited equivalent or higher binding than 1G01 (Figure 1B). We next tested if our mAbs target the NA catalytic site and compete with 1G01 for NA binding. A binding competition assay by using biolayer interferometry (BLI) revealed that none of the six mAbs showed any appreciable competition with 1G01, indicating that they recognize antigenic surfaces distinct from the conserved catalytic site (Figure 1C). To better understand their binding specificities, we generated fragment antigen-binding (Fab) from NDS.1, NDS.1.1, NDS.3, NDS.5, and NDS.6 and measured binding affinity of that to soluble recombinant N2 tetramers by BLI (Figures 1D and S1C; Table S2). Fabs of NDS.1, NDS.1.1, NDS.3, and NDS.5 showed sub-nanomolar to weaker nanomolar affinity to all tested NAs (Figures 1D and S1C). The Fab of NDS.1.1 had similar overall affinity yet a noticeably faster off-rate for A/Wisconsin/67/2005 (WI05) and A/Darwin/6/2021 (DW21) NAs, compared with NDS.1, NDS.3, and NDS.5 Fabs. Among tested Fabs, NDS.6 had the weakest affinity to all but A/Moscow/10/1999 (MO99) NA and no interpretable binding to WI05 NA (Figures 1D and S1C), and it was therefore excluded from further analyses. To our surprise, both NDS.1.1 and NDS.3 Fabs showed the highest affinity to the NA of swine-origin H3N2v virus A/Indiana/10/2011 (IN11v). We also confirmed that all tested mAbs were N2-specific and did not cross-react with other group 1 or group 2 NA subtypes (Table S3). In summary, we isolated six mAbs from H3N2-infected individuals, which recognize conserved epitopes among N2 subtype NAs outside the catalytic site.

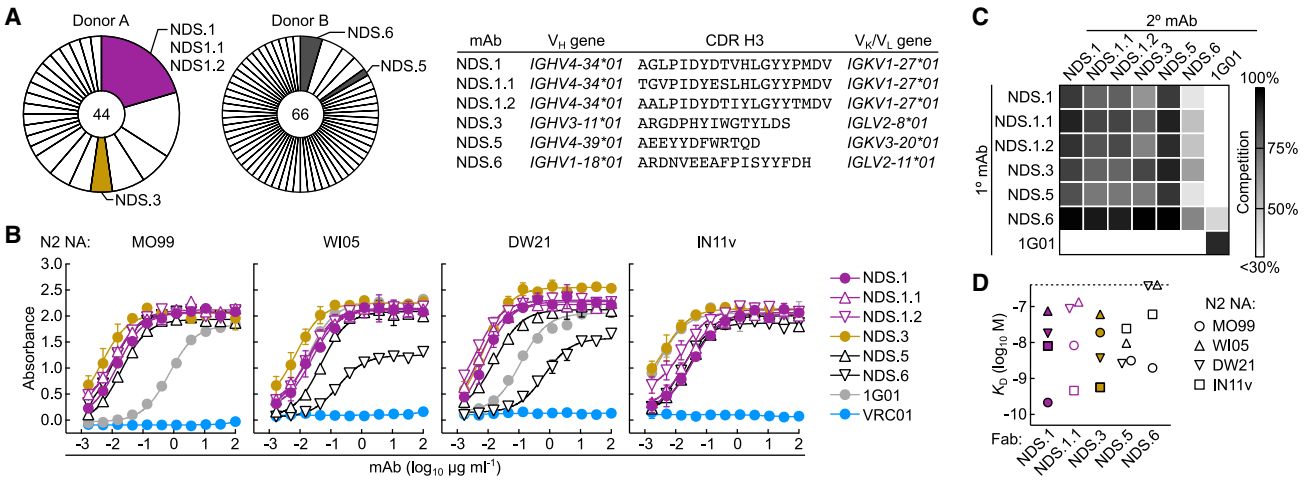

Figure 1. Identification and characterization of broadly cross-reactive N2 NA-targeting antibodies

(A) Immunogenetics of N2-specific B cells. Immunoglobulin variable heavy- and light-chain gene usage and V-D-J junction of NA-specific B cells for two donors are shown. Each pie slice indicates a B cell clone with the same V_H and V_K/V_L gene usage and similar CDR H3 identity. The total number of paired heavy- and light-chain sequences analyzed is shown inside each pie chart. Immunoglobulin gene usage and CDR H3 sequences of NA dark side-directed mAbs we characterized are shown.

(B) ELISA binding curves of dark side-directed mAbs against recombinant N2 protein of A/Moscow/10/1999 (H3N2, MO99); A/Wisconsin/67/2005 (WI05, H3N2); A/Darwin/6/2021 (DW21, H3N2); and A/Indiana/10/2011 (IN11v, H3N2v). Broadly cross-reactive NA catalytic site-specific mAb 1G01 and non-targeting (HIV-1 Env-specific) mAb VRC01 were used as positive and negative controls, respectively. Data are plotted as mean ± SD.

(C) Cross-competition profile of NA-targeting mAbs, shown as a heatmap. Binding was measured by BLI with recombinant WI05 N2 protein and full IgG.

(D) Binding affinity of Fab of dark side-directed mAbs to recombinant N2 NAs. Binding kinetics of Fabs were measured by BLI with recombinant MO99, WI05, DW21, and IN11v NAs. K_D values calculated using the Langmuir 1:1 interaction model for each Fab-NA pair are shown.

See also Figure S1 and Tables S1–S3.

Cryo-EM structures of Fabs NDS.1 and NDS.3 in complex with NA

To identify the epitopes recognized by mAbs NDS.1 and NDS.3 and to elucidate the structural basis of their broad N2 specificity, we determined cryo-EM structures of Fab NDS.1 in complex with N2 IN11v NA and of Fab NDS.3 in complex with N2 DW21 NA (Table S4). For structural studies, we chose two different NAs that produced a stable ternary complex with NDS.1 and 1G01 Fabs and a binary complex with NDS.3 Fab to learn how these mAbs recognize the NA of the contemporary human H3N2 as well as the antigenically divergent swine-origin H3N2v. 1G01,[15] which targets the catalytic site of NA from the top of the mushroom-shaped NA globular head, was added to the IN11v-NDS.1 complex to overcome the preferred orientation of particles in vitrified ice (Figure S2). The 3.0 Å cryo-EM map of this ternary complex revealed that the NDS.1 and 1G01 Fabs bind on opposite sides of NA, with four NDS.1 Fabs bound to the underside of the NA globular head (Figure 2A). Each NDS.1 Fab interacted with a single NA protomer and was positioned at a slight upward angle to the horizontal plane of the tetramer, with the constant region extending outward from under the head. The cryo-EM density for NDS.1 was weaker than the rest of the consensus map owing to partial Fab occupancy. To improve the NDS.1 density, we performed symmetry expansion and signal subtraction outside a mask encompassing one NA protomer with the two bound Fabs (1G01 and NDS.1), which were followed by 3D classification within a mask encompassing the target Fab to isolate the subset of complexes with occupied NDS.1 Fab (Figures S2 and S3). Subsequent local refinement produced a 3.6 Å map with strong NDS.1 density, which allowed us to build an atomic model of the NDS.1-NA complex (Figures 2B and 2C). Despite only the heavy chain of NDS.1 contributing to the interaction interface, the total buried surface areas on NA and the Fab were relatively large (1,014 and 1,118 Å^2, respectively). Of the six four-stranded β sheets forming the NA molecule,[33] NDS.1 targeted the bottom regions of β sheets IV and V, with some additional interactions with the N terminus (β sheet VI; Figure 2C). CDR H1 as well as a portion of the 17-residue long CDR H3 were positioned along a crevice in the underside surface of the NA protomer, with three bulky aromatic residues (Phe31, Tyr100F, and Tyr100G in Kabat numbering scheme), along with Ser28 and Asn30, filling the crevice (Figure 2D). CDR H1 and CDR H3 contributed 378 and 386 Å^2, respectively, to the total buried surface area on the Fab, whereas the contribution of CDR H2 was minor (54 Å^2). In addition to the CDRs, two framework regions (FRs) of the heavy chain interacted with NA, including residues 1–3 of FR H1 and residues 73–77 of FR H3 (Figure 2D). These two regions flanked CDR H1, creating the remainder of the paratope, with buried surface areas of 179 and 122 Å^2, respectively (total FRs contribution of 27%). In total, 14 hydrogen bonds between NDS.1 and IN11v NA were observed, involving side-chain as well as main-chain atoms on both sides (Figure 2E).

The cryo-EM structure of NDS.3 Fab in complex with DW21 NA was solved to a resolution of 2.7 Å (Figures 3A and S4; Table S4). Fab NDS.3 also targeted the underside of the NA globular head, approaching NA upward at an angle of about 30° to the horizontal plane of the tetramer (Figure 3B). It interacted primarily with β sheet III of NA (Figure 3C), as well as with one β strand each of β sheets II and IV that were adjacent to β sheet III. Each of the four bound Fabs contacted mainly the

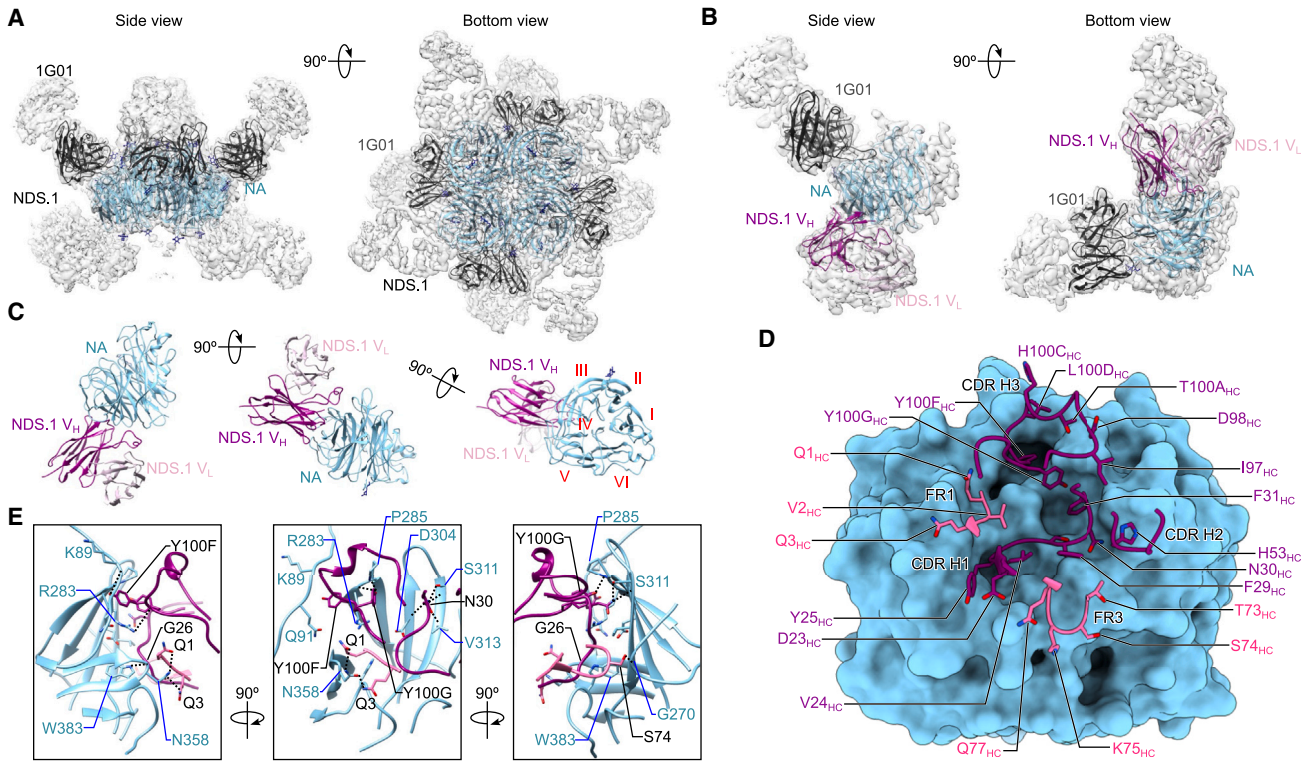

Figure 2. Cryo-EM structure of NDS.1 and 1G01 Fabs in complex with IN11v N2 NA

(A) Consensus cryo-EM map of IN11v N2 NA with bound NDS.1 and 1G01 Fabs, with docked atomic models of NA and 1G01 colored light blue and gray, respectively. Glycans are shown in stick representation. The cryo-EM density for NDS.1 is weaker due to partial occupancy.

(B) Local 3D classification and refinement of a region containing one NA protomer with two bound Fabs. The heavy and light chains of NDS.1 are colored dark magenta and light pink, respectively.

(C) Ribbon diagram of the NA-NDS.1 complex. Coloring is as in (B). Only the heavy chain of NDS.1 interacts with NA. The six four-stranded β sheets forming the structure of the NA monomer are labeled with Roman numerals.

(D) Contact interface between NA and NDS.1. IN11v N2 NA is shown in surface representation. The CDRs and framework regions (FRs) of the NDS.1 heavy chain participating in the interaction are depicted as ribbons, with residues in contact with NA shown in stick representation and labeled. The FRs are colored hot pink.

(E) Detailed illustration of the interactions between NA and NDS.1. Only the molecular regions participating in the interaction are shown for clarity. Residues forming hydrogen bonds are shown in stick representation and labeled in light blue and black for NA and NDS.1, respectively. Dashed lines depict hydrogen bonds.

See also Figures S2 and S3 and Table S4.

side and bottom regions of one NA protomer, burying 898 and 933 Å^2 on the NA and Fab surfaces, respectively (Figure 3A). CDR H1 and CDR H3 were situated close to the inter-protomer interface of NA, resulting in residues Asp31, His98, and Tyr99 forming a small additional interface (buried surface areas on NA and Fab of 63 and 64 Å^2, respectively) with a neighboring NA protomer (protomer 2) (Figures 3B–3D). All the CDRs of the heavy and light chains of NDS.3 participated in the interaction with the primary protomer 1, which involved multiple polar and charged contacts (Figure 3D). The CDRs of the heavy chain accounted for the majority of the buried surface area on the NA (66%, 634 Å^2), contributing four salt bridges (between Asp31^{HC} and Lys261, Arg55^{HC} and Glu258, and His98^{HC} and Asp213) and seven hydrogen bonds to the interaction interface with protomer 1 (Figure 3E). Furthermore, aromatic residues Tyr50 and Phe58 of CDR H2 and Tyr99 and Trp100A of CDR H3 engaged in hydrophobic contacts with NA residues and provided additional shape complementarity. The CDRs of the light chain formed one salt bridge (between Asp27B^{LC} and Lys267) and five hydrogen bonds, covering 328 Å^2 on NA protomer 1.

NDS.1 and NDS.3 epitope comparison and conservation

We found that the structures of IN11v and DW21 NAs were highly similar to each other (root-mean-square deviation in C_α atom positions of 0.54 Å). This allowed us to compare the epitopes of NDS.1 and NDS.3 by superposing the two NA molecules. The two antibodies targeted different but adjacent areas on the NA underside, with their epitope outlines sharing a border (Figures 4A and 4B). The four NA residues that contributed to both epitopes included Ser269, located in the loop connecting β sheets III and IV, as well as Asn309 (IN11v)/Asp309 (DW21), Ser311, and Ile312, belonging to β sheet IV. The contacts formed by these residues were mainly limited to van der Waals interactions, with the exception of one hydrogen bond between the backbone nitrogen of Ile312 of NA and the side-chain oxygen of Ser94 of the NDS.3 light chain, and two hydrogen bonds between the side-chain nitrogen of Asn30 of the NDS.1 heavy chain

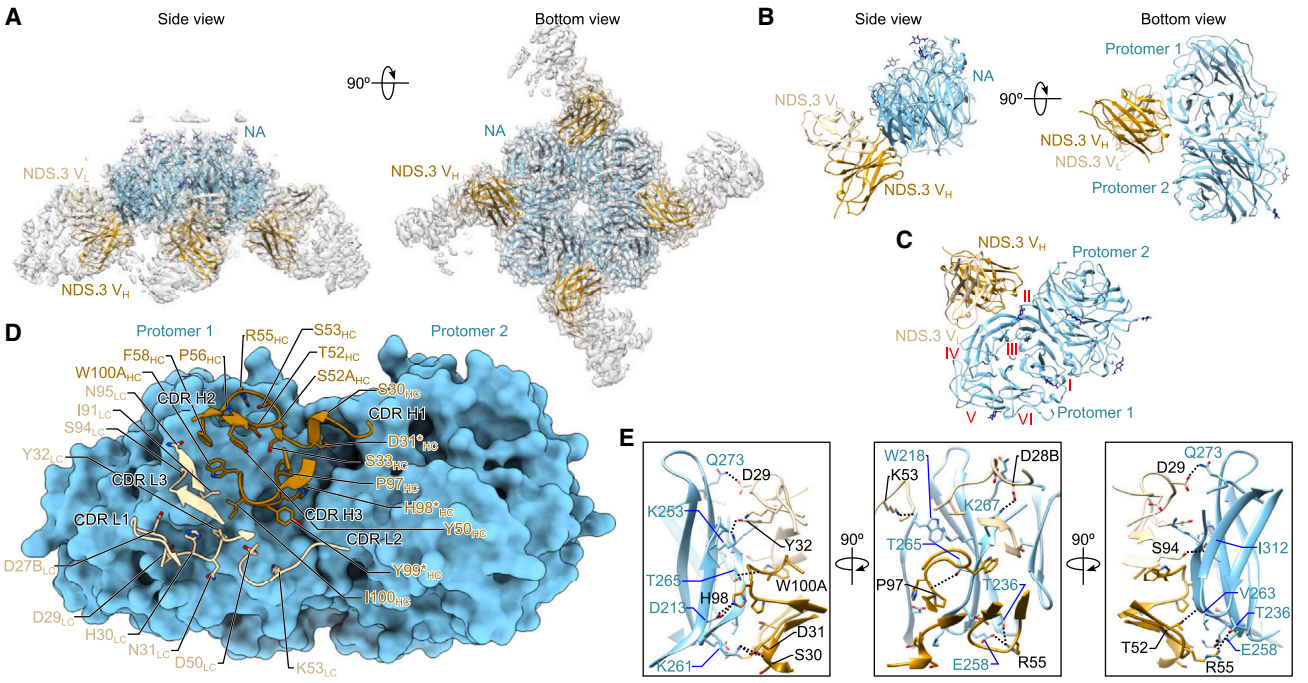

Figure 3. Cryo-EM structure of NDS.3 Fab in complex with DW21 N2 NA

(A) Cryo-EM map and docked atomic models of DW21 N2 NA in complex with NDS.3 Fab. The heavy and light chains of NDS.3 are colored dark gold and light gold, respectively. NA is colored light blue. Glycans are shown in stick representation.

(B) Ribbon diagram of the NA-NDS.3 complex. Coloring is as in (A).

(C) Fab NDS.3 interacts primarily with β sheet III of NA. NA orientation is the same as in Figure 2C, right.

(D) Contact interface between NA and NDS.3. DW21 N2 NA is shown in surface representation. The CDRs of Fab NDS.3 are depicted as ribbons and labeled, with residues in contact with NA shown as sticks and labeled. Asterisks denote NDS.3 residues contacting both NA protomers.

(E) Detailed illustration of the interactions between protomer 1 of NA and Fab NDS.3. Only the molecular regions participating in the interaction are shown for clarity. Residues forming hydrogen bonds and salt bridges are shown in stick representation and labeled in light blue and black for NA and NDS.3, respectively. Dashed lines depict hydrogen bonds and salt bridges.

See also Figure S4 and Table S4.

and the backbone oxygen and side-chain oxygen of NA Ser311 (Figure 4C). The four NA residues participating in both epitopes maintained the same positions in the two structures, and superposition of the IN11v-NDS.1 and DW21-NDS.3 complexes revealed no clashes between the two Fabs (Figure 4B). Indeed, we did not observe cross-competition for NA binding when Fabs of NDS.1 and NDS.3 were used instead of IgG (Figure S5). Together, NDS.1 and NDS.3 epitopes cover a large surface on the NA underside, and the two epitopes are not overlapping (Figure 4D).

The epitopes of NDS.1 and NDS.3 appeared well conserved among human seasonal H3N2 viruses, spanning more than 50 years of antigenic evolution (Item S1). The majority of the residues on NA contacting NDS.1 (33/37, 89%) and NDS.3 (26/31, 84%) had virtually no variation among 188 non-redundant representative NA sequences of seasonal human H3N2 viruses (Figure 4E). Substitution at position 267, one of the most variable residues within the NDS.3 epitope, from Lys (DW21) to Thr (IN11v), which is predicted to eliminate a salt bridge with Asp27B^{LC}, did not have a major impact on its recognition by NDS.3 (Figure 1D). The epitopes of NDS.1 and NDS.3 were still well conserved (30/37, 81% and 25/31, 81% for NDS.1 and NDS.3, respectively) when we use 80 non-redundant representative N2 sequences of HxN2 viruses, including H1N2, H2N2, H3N2, H7N2, and H9N2 (Figure 4E; Item S2). This suggests that the cross-reactivity of NDS.1 and NDS.3 may extend beyond H3N2 viruses. Overall, we found that both the NDS.1 and NDS.3 epitopes are largely conserved among human H3N2 viruses and also across HxN2 viruses.

Biological activity of NA dark side-targeting antibodies

We next assessed the functionality of the NA dark side-targeting antibodies using both recombinant NA proteins and viruses. It is known that the catalytic activity of NA can be blocked not only by directly targeting the catalytic pocket but also through steric hindrance by antibody binding to nearby sites on NA or even the stem of neighboring HA molecules.[34,35] We first measured the NA inhibitory (NAI) activity of the dark side-targeting antibodies by influenza replication inhibition NA-based assay (IRINA),[36] which detects the enzymatic activity of NA expressed on the surface of influenza-infected cells. The IRINA is a direct, functional enzymatic assay that measures NA catalytic activity through the release of the fluorogenic end product 4-methylumbelliferone from the non-fluorescent small-molecule substrate 2′-(4-methylumbelliferyl)-α-D-N-acetylneuraminic acid (MUNANA). NAI activity is therefore only observed in the IRINA for antibodies that directly compete with substrate binding to the catalytic site. As expected, while the catalytic site-directed 1G01 showed NAI activity

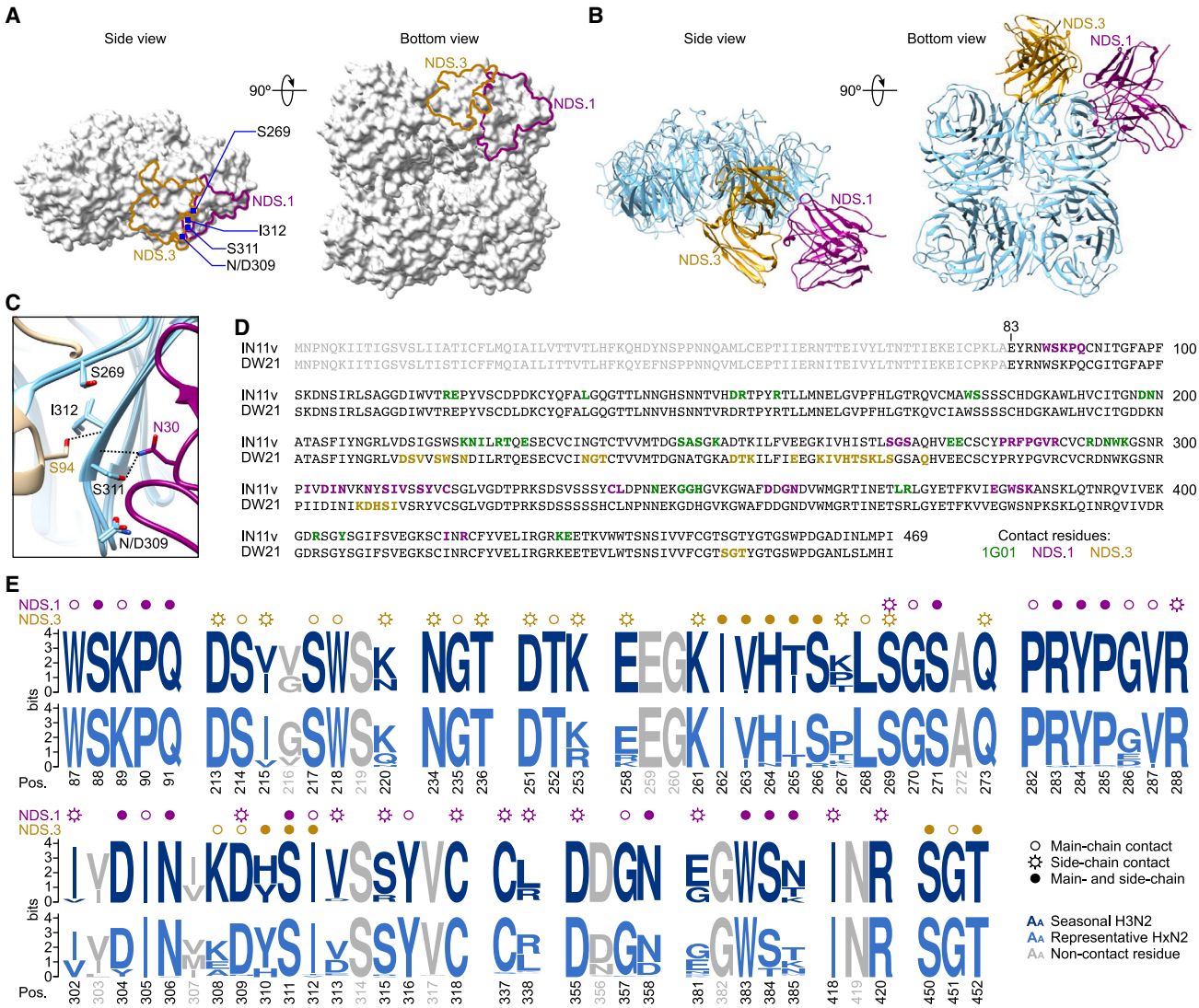

Figure 4. NA underside epitopes recognized by NDS.1 and NDS.3

(A) Surface representation of the NA head tetramer with the epitopes of NDS.1 and NDS.3 outlined in dark magenta and gold, respectively. Blue dots indicate the positions of the NA residues that contribute to both epitopes. Epitopes are shown only on one NA protomer for clarity.

(B) Ribbon diagram showing Fabs of NDS.1 (dark magenta) and NDS.3 (gold) interacting with NA tetramer (light blue). Bound Fabs are shown only on one NA protomer for clarity.

(C) NA residues contributing to both NDS.1 and NDS.3 epitopes. NA, NDS.1 heavy chain, and NDS.3 light chain are colored in light blue, dark magenta, and light gold, respectively. Dashed lines depict hydrogen bonds.

(D) Sequence alignment of NAs of IN11v and DW21. Residues forming the epitopes of 1G01, NDS.1, and NDS.3 are colored in green, dark magenta, and gold, respectively. Gray residues (positions 1–82) are part of the transmembrane and stalk region and were not included in the recombinant soluble NA tetramers used for structural studies.

(E) Sequence conservation of NDS.1 and NDS.3 epitopes among NAs of human H3N2 (dark blue) and HxN2 (sky blue). NDS.1 and NDS.3 contact residues are indicated above the sequence logo plots. Open circles denote contacts formed by NA main-chain atoms only; open circles with rays denote side-chain contacts only; filled circles denote both main- and side-chain contacts. Gray residues are not part of the epitopes.

See also Figure S5.

in this assay, all of our mAbs targeting the NA dark side showed no NAI activity to four H3N2 viruses tested (Figure 5A). To better understand the biological relevance of the dark side-targeting antibodies, we also performed the enzyme-linked lectin assay (ELLA). ELLA measures the cleavage of sialic acid from the glycoprotein fetuin by NA, which can be inhibited by antibodies not only binding directly to the catalytic site but also through steric hindrance, unlike the IRINA.[37] All the dark side-directed mAbs showed NAI activity comparable to the control antibody 1G01 to three human H3N2 viruses, except NDS.5 that showed weaker NAI. Further, potent NAI activity of NDS.1, NDS.1.1, and NDS.3 was detected against non-human H3N2 influenza virus A/duck/France/161005/2016 (Figure 5B). We also measured NAI activity against several non-H3N2 influenza viruses in ELLA, including

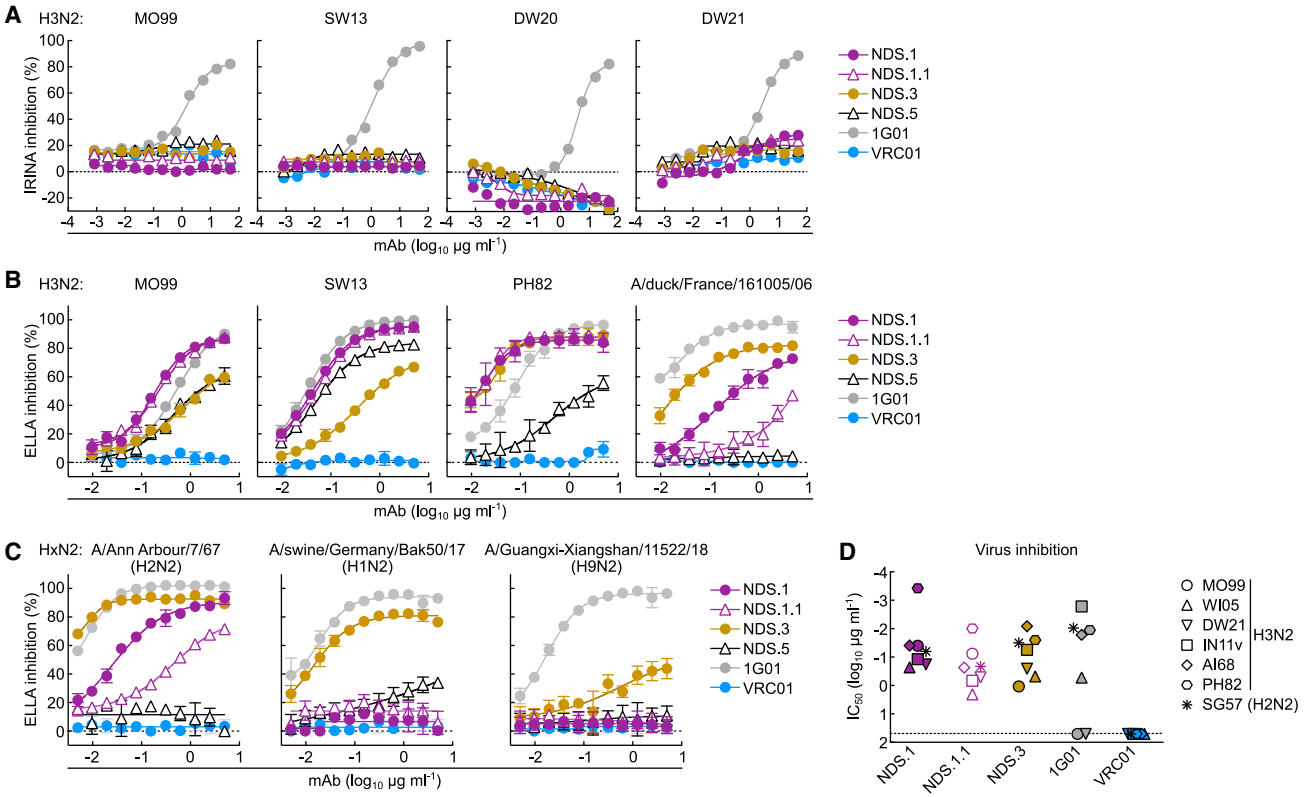

Figure 5. *In vitro* virus inhibition by NA dark side-directed mAbs

(A) NAI activity of the mAbs against H3N2 viruses measured by IRINA. SW13, A/Switzerland/9715293/2013 (H3N2); DW20, A/Darwin/106/2020 (H3N2). Broadly cross-reactive NA catalytic site-specific mAb 1G01 and non-targeting (HIV-1 Env-specific) mAb VRC01 were used as positive and negative controls, respectively. Data are plotted as mean ± SD.

(B) NAI activity of the mAbs against H3N2 viruses measured by ELLA. PH82, A/Philippines/2/1982 (H3N2). Data are plotted as mean ± SD.

(C) NAI activity of the mAbs against HxN2 viruses measured by ELLA. Data are plotted as mean ± SD.

(D) Viral growth inhibition of the mAbs against H3N2, H3N2v, and H2N2 viruses. The half-maximal inhibitory concentration (IC_{50}) of mAb for each virus was calculated from two independent experiments, and mean IC_{50} values for each mAb-virus combination are shown. AI68, A/Aichi/2/1968 (H3N2); SG57, A/Singapore/1/1957 (H2N2).

See also Figure S7.

A/Ann Arbor/7/1967 (H2N2), A/swine/Germany/Bak50/2017 (H1N2), and A/Guangxi-Xiangshan/11522/2018 (H9N2). Although potent NAI activity was found against A/Ann Arbor/7/1967 (H2N2) for all dark side-directed mAbs, only NDS.3 showed strong activity against A/Swine/Germany/Bak50/2017 (H1N2) and modest activity against A/Guangxi-Xiangshan/11522/2018 (H9N2) in ELLA (Figure 5C). This demonstrates that the NA dark side-directed mAbs are able to inhibit NA catalytic activity by sterically hindering access to glycoprotein substrates.

While NA-directed antibodies do not typically block viral entry to host cells, they inhibit viral egress of nascent particles from the infected cells through inhibition of NA catalytic activity.[10,38] Therefore, we assessed the ability of NA dark side-directed mAbs to inhibit *in vitro* viral growth of five H3N2 viruses, one H3N2v virus, and one H2N2 virus. The virus growth inhibition assay was performed using reporter influenza viruses to detect infected cells over time.[39] In this assay, mAbs were first incubated with viruses prior to adding to the substrate cells. The virus inoculum was removed after 4–5 h, and cells were kept in culture media supplemented with mAbs for another 24–28 h. In order to calculate viral growth inhibition, we normalized it to inhibition by the NA inhibitor zanamivir (100% inhibition). We found that all NA dark side-directed mAbs inhibited the growth of all viruses tested, including non-circulating H3N2v and H2N2 viruses (Figure 5D). The control antibody 1G01 did not inhibit growth of the MO99 and DW21 H3N2 viruses, whereas all dark side-directed mAbs potently inhibited those viruses. Based on these results, we showed that the NA dark side-directed mAbs are capable of inhibiting not only a wide range of H3N2 viruses but also divergent H3N2v and H2N2 viruses, by targeting highly conserved epitopes on the NA underside.

Prevalence of NA dark side-directed antibody

Since we isolated dark side-directed mAbs from convalescent human PBMCs, we hypothesized that dark side-directed antibodies were also present in the convalescent sera at the same time point. To selectively detect dark side-directed antibodies within polyclonal sera, we designed recombinant NA proteins that harbor engineered glycans on the underside of NA to sterically block the access of dark side-directed mAbs. After

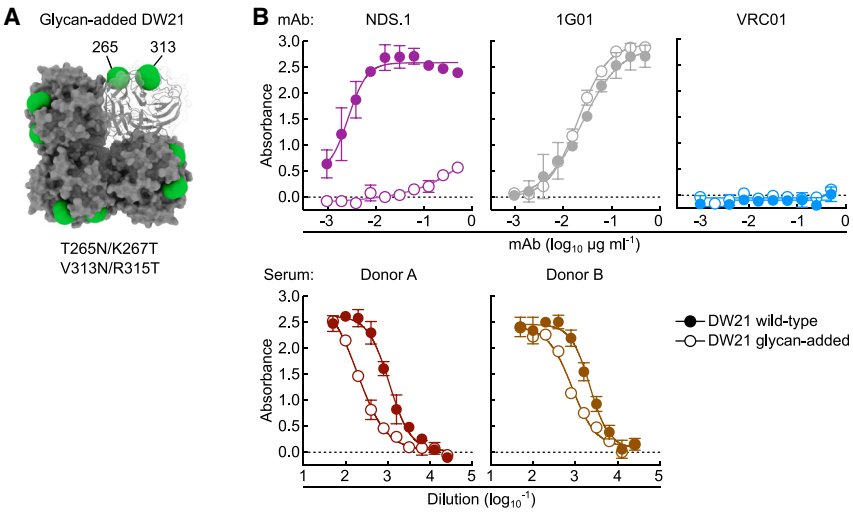

Figure 6. NA dark side-directed antibodies in human convalescent serum and plasma samples

(A) Glycan-added DW21 N2 NA. Locations of the additional N-linked glycosylation sites are shown as green spheres (bottom view). Amino acid substitutions introduced in the glycan-added DW21 NA are indicated.

(B) ELISA using a pair of DW21 wild-type (WT) and glycan-added NAs. mAb-binding profile of DW21 WT and glycan-added NAs (top). Broadly cross-reactive NA catalytic site-specific mAb 1G01 and non-targeting (HIV-1 Env-specific) mAb VRC01 were used as positive and negative controls, respectively. Serum (donor A) and plasma (donor B) antibody-binding profile of DW21 WT and glycan-added NAs (bottom). Differences between WT and glycan-added NAs correspond to the amount of the dark side-directed antibodies in given samples. Data are plotted as mean ± SD.

See also Figure S6.

screening various glycan positions and combinations, we found that a double-glycan-added DW21 NA (T265N/K267T and V313N/R315T) had the desired antigenic profile, with severely reduced binding to our dark side-directed mAb while retaining the reactivity to 1G01 (Figure 6A). By using a pair of glycan-added and unmodified wild-type (WT) DW21 NAs, we observed that the convalescent serum and plasma sample of donor A and B, respectively, had substantially reduced binding to the glycan-added NA, compared with WT NA (Figure 6B). These results indicate that there was a detectable amount of dark side-targeting antibodies in the circulation of both donors.

We next searched for potential dark side-directed antibodies in the literature to gauge the generalizability of such antibodies upon influenza infection or vaccination beyond the two individuals we studied. We found a mAb named 229-2G05 isolated from an H3N2-infected donor in Chen et al.,[4] which had a remarkably similar biological activity profile to our dark side-directed mAbs. 229-2G05 is N2-specific, and its NAI activity can only be measured in ELLA but not in NA-star assay (which uses a small-molecule substrate similar to MUNANA).[4] We made Fab of 229-2G05 and structurally characterized it in a complex with DW21 NA by cryo-EM and found that it recognized a dark side epitope similar to that of NDS.3 (Figures S6A and S6B). Indeed, 229-2G05 had severely reduced binding to the glycan-added DW21 NA (Figure S6C). Moreover, we characterized NDS.5 in complex with DW21 NA by negative-stain EM and found that it binds to an NDS.1-like epitope, although its angle of approach is almost perpendicular to the NA tetramer plane (Figure S6D). The identification of two additional dark side-directed mAbs from two independent human subjects targeting epitopes that overlap with either NDS.1 or NDS.3 highlights that dark side-directed antibodies may be commonly elicited by infection or vaccination.

NA dark side-directed mAbs confer protection against lethal H3N2 influenza virus challenge in mice

To see if the *in vitro* inhibitory activity of the NA dark side-directed mAbs can translate into *in vivo* efficacy, we conducted a series of lethal influenza virus challenge studies in mice. First, we assessed protective efficacy in a prophylactic setting where the mAbs were given 24 h prior to challenge with A/Philippines/2/1982 (H3N2) virus (10 × 50% lethal dose [LD_{50}]). In this model, NDS.1 conferred full protection without any noticeable body weight loss when 10 and 3 mg kg^{-1} were administered, and it afforded 90% survival when given the lowest dose of 1 mg kg^{-1} (Figure 7A; Table S5). NDS.1.1 showed similar performance as NDS.1, providing 80%–90% protection with all doses tested. NDS.3 conferred full protection with a dose of 10 and 3 mg kg^{-1}, although there was ~8% mean body weight loss at days 8 and 9 when given 3 mg kg^{-1}. However, this mAb afforded only 10% survival when the lowest amount (1 mg kg^{-1}) was administered (Figure 7A). Consistent with a previous report,[15] the catalytic site-directed 1G01 conferred full protection at all doses tested. The control anti-HA stem mAb FI6v3[40] provided weaker protection, compared with all tested anti-NA mAbs. Full protection was observed when the highest 10 mg kg^{-1} of FI6v3 was given, but protective efficacy rapidly dropped as the mAb dose decreased (Figure 7A). Overall, NA dark side-directed mAbs provided potent protection from mortality and morbidity caused by H3N2 virus infection in mice when prophylactically administered.

Since commercial antivirals targeting influenza virus NA are efficacious as therapeutics after symptom onset, we sought to assess protective efficacy of the dark side-directed mAbs in a post-exposure therapeutic setting. Mice were infected with a 5 × LD_{50} of A/Philippines/2/1982 (H3N2) virus 48 h prior to administration of mAbs at 10 mg kg^{-1}. In this setting, mice did not show appreciable body weight loss at the time of mAb administration. Overall, 90% of mice receiving either NDS.1 or NDS.1.1 survived, with a mild body weight loss of ~10%, which was similar to that of the control 1G01-treated mice, whereas NDS.3-treated mice resulted in 50% survival with more severe body weight loss (Figure 7B; Table S5). The control anti-HA mAb FI6v3 afforded only partial protection (30% survival) in this therapeutic setting. We showed that the NA dark side-directed mAbs were highly protective not only when given as pre-exposure prophylaxis, even at a dose as low as 1 mg kg^{-1}, but also as post-exposure therapeutics in a mouse model.

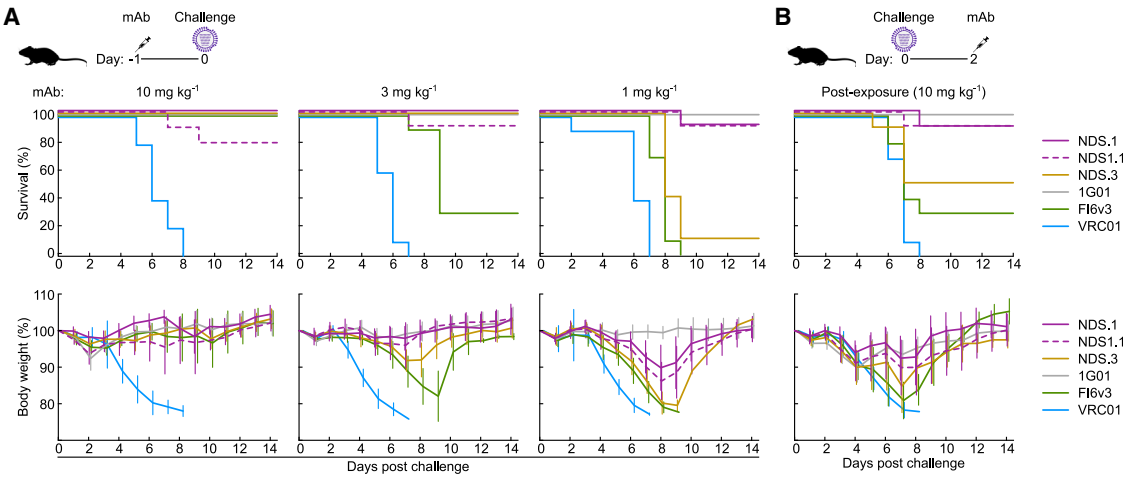

Figure 7. Protective efficacy of the NA dark side-directed mAbs against A/Philippines/2/1982 (H3N2)

(A) Pre-exposure prophylaxis experiment. BALB/c mice were treated with 10, 3, or 1 mg kg^{-1} of mAbs intraperitoneally 24 h prior to the intranasal virus challenge. Virus dose was 10 × LD_{50}. Group size was 10 except for NDS.1 at 1 mg kg^{-1} (n = 9). Percent survival (upper) and percent body weight change (lower) are shown. (B) Post-exposure treatment experiment. BALB/c mice were infected with virus prior to mAb administration (10 mg kg^{-1}) at 48 h post-infection. Virus dose was 5 × LD_{50}. Group size was 10 except for NDS.1 group (n = 9). Percent survival (upper) and percent body weight change are shown. Error bars indicate SD. See also Table S5 for statistical analyses of Kaplan-Meier curves.

In addition, we characterized the dark side-directed mAbs for their ability to retain binding to NAs that contain antiviral resistant mutations. For this, we designed recombinant DW21 NA containing the E119V/I222L mutations, which have been shown to escape zanamivir.[41] We measured binding of dark side-directed mAbs and catalytic site mAbs to DW21 N2 with and without the E119V/I222L mutations by ELISA. As expected, the catalytic site-directed mAb binds substantially weaker to the NA with the substitutions while the dark side-directed mAbs retain their binding to DW21 N2 with the E119V/I222L mutations (Figure S7), highlighting the potential of dark side-directed mAbs as antiviral countermeasures for drug-resistant viruses.

DISCUSSION

Influenza virus NA has long been central to drug discovery efforts, with licensed antivirals targeting NA continuing to save countless lives since their first approval in 1999. Although it has been known, since the 1980s, that antibodies can inhibit the catalytic activity of NA, only a few mAbs have been identified in humans to date that recapitulate the molecular interactions of sialoside substrates and possess similar breadth of reactivity as commercial NA inhibitors.[14,15,42] Besides these rare mAbs, antibodies to antigenic sites peripheral to the catalytic site can also inhibit NA activity by sterically hindering access to sialoside substrates, but those antibodies are generally less cross-reactive.[43] Antibodies such as CD6 and NA-22 recognize the lateral surface of the NA globular head distant from its catalytic site, yet still inhibit the catalytic activity of NA through indirect steric hindrance.[21–23] Finally, a few reports have noted that the catalytic activity of NA can also be inhibited through anti-HA stem antibodies through steric hindrance.[34,35] Nevertheless, our understanding of the NA antigenic landscape is still far from complete. The first suggestion of an antigenic site on the NA underside was made by Webster et al. in 1984, in which the authors defined antigenic area 1 (region 1) based on apparent antigenic drift.[32] Nearly four decades later, we here rediscovered the NA dark side antigenic site by isolating and characterizing human mAbs that define two non-overlapping epitopes on the NA underside. It is fascinating that although the region 1 mAbs reported earlier had very limited biological activity,[32] the dark side-directed mAbs reported here had broad NAI activity and protective efficacy *in vivo*, accentuating the incompleteness of our understanding of the antigenic landscape of NA. While these NA dark side-targeting mAbs are N2 subtype-specific, it is likely that antigenic sites corresponding to these epitopes exist on other NA subtypes such as N1.

It would be surprising to find functional mAbs targeting the NA underside if the mushroom-shaped NA molecule formed static closed tetramers on the viral surface; however, a study describing the mesoscale all-atom molecular dynamics simulations of whole influenza virions has provided new insights into this potential paradox.[25] In addition to the two known motions of HA (i.e., breathing and tilting), simulations revealed a third dynamic behavior of influenza virus glycoproteins: NA tilting. We found that tilting of the NA head during the simulations allowed NDS.1 to access its epitope, providing a plausible explanation for the elicitation and functionality of dark side-targeting antibodies. Another important consideration is that the tetrameric NA globular head may exhibit greater heterogeneity than is believed. We show the spontaneous dissociation of NA globular head domains in the context of recombinant NA proteins bearing commonly used tetramerization domains.[29] This behavior of dissociating a tetramer into four monomers or two dimers is also found in distantly related paramyxovirus hemagglutinin-neuraminidases (HNs).[44–46] The viral attachment G protein of Nipah virus, a member of the six-bladed β propeller fold homotetrameric NA/sialidase-like proteins, has revealed a distinctive two-heads-up and two-heads-down conformation that is different from other known paramyxovirus NAs/sialidases

structures,[28] illustrating how antigenic surfaces, including the dark side, are exposed to the immune system. Another intriguing structural feature of the parainfluenza virus 3 HN was reported[47] where a protomer of a dimer is interacting with the neighboring viral fusion protein through its surface apart from the sialidase center, suggesting that surfaces distant from the catalytic site can play functional roles and be viable targets for antibodies to disrupt viral functions. It is possible that the influenza NA exhibits some conformational heterogeneity in addition to its extreme tilting on the viral surface and hence exposes the dark side as well as tetramer interface epitopes much more than the stereotypic view of the static mushroom-like structure would suggest.

Several potent anti-NA mAbs were isolated from plasmablasts of either H1N1- or H3N2-infected individuals, but NA-targeting plasmablast responses were barely detectable in vaccinated individuals, suggesting that NA in current influenza vaccines is poorly immunogenic.[4] While the dark side-directed mAbs described here were isolated from two convalescent donors, most functional mAbs were isolated from donor A who was born in the 1950s. It is not possible to know if the B cell lineages we characterized here were induced by infection with (or exposure to) the historical H2N2 virus that circulated between 1957 and 1968 or the H3N2 virus (since 1968). Regardless, it is fascinating that the B cell lineages specific to the NA dark side responded to the recent H3N2 virus infection in the individual, and they broadly cross-react with N2 NA from human H3N2 and H2N2 viruses and several zoonotic HxN2 viruses. Given the degree of somatic hypermuation (SHM) in the dark side-directed antibodies, we anticipate that vaccine elicitation of such antibodies can be achievable with appropriate immunogens. We have shown that the dark side-directed mAbs can inhibit the catalytic activity of NA on the virus when a macromolecular substrate (i.e., fetuin) was used, likely through indirect steric hindrance, and blocked virus propagation and spread *in vitro* through inhibition of its sialidase activity. These viral inhibitory properties of the dark side-directed mAbs are analogous to the NA inhibitors such as oseltamivir and zanamivir or the catalytic site-directed antibodies such as 1G01, DA03E17, and FNI9,[14,15,42] and they all can confer both pre- and post-exposure prophylactic protection in murine infection model of influenza. Additionally, the hallmark substitutions associated with resistance to oseltamivir and/or zanamivir such as E119V and I222L[41] did not impact the dark side epitopes. We noticed that the within-subtype breadth of the dark side-directed mAbs appears somewhat superior to that of 1G01, although the latter cross-reacts with other NA subtypes as well. A similar hierarchy has been seen with HA head-directed mAbs (i.e., lateral patch-directed mAbs are superior within a subtype to receptor-binding site-directed mAbs, while the latter go beyond subtype boundaries). Identification of additional protective antigenic sites is an important step toward developing effective vaccines and therapeutics against this ever-evolving virus. Our findings, along with two other reports that have described human mAbs to either the underside or lateral side of NA,[48,49] define additional viable sites of vulnerability on influenza virus NA and will foster new multipronged vaccine/therapeutic approaches targeting multiple sites of vulnerability on HA, NA, and potentially other viral proteins.

Limitations of the study

Our study evaluated mAb treatment only at 24 h prior to infection and 48 h post-infection. Given that experimental influenza virus infection in mice does not recapitulate disease course of human influenza, animal models that reflect human diseases such as macaques would be needed for further evaluation of mAbs as prophylaxis and/or therapeutic countermeasures. We observed clonal expansion of B cells targeting the dark side epitope in donor A with V_H4-34 germline gene, which is known to associate with polyreactivity and B cell anergy. A larger study is necessary to understand if this gene is recurrently used in different individuals and exhibits polyreactivity. While synergy between NA catalytic site-directed mAb and HA stem-directed mAb have been shown[42], studying synergy between two NA-targeting mAbs (e.g., catalytic site and dark side) or between HA- and NA dark side-directed mAbs would aid in developing a therapeutic cocktail targeting multiple sites of vulnerability of influenza virus and minimizing the risk of generating escape variants.

STAR★METHODS

Detailed methods are provided in the online version of this paper and include the following:

- KEY RESOURCES TABLE
- RESOURCE AVAILABILITY
  - Lead contact
  - Materials availability
  - Data and code availability
- EXPERIMENTAL MODEL AND STUDY PARTICIPANT DETAILS
  - Human specimens
  - Mice
- METHOD DETAILS
  - Single-cell sorting, immunoglobulin amplification, sequencing and mAb production
  - Cell lines
  - Viruses
  - Protein expression and purification
  - NA sequence analysis
  - Enzyme-linked immunosorbent assay (ELISA)
  - Biolayer Interferometry (BLI)
  - Influenza replication inhibition neuraminidase-based assay (IRINA)
  - Enzyme-linked lectin assay (ELLA)
  - Virus Inhibition assay
  - Passive transfer
  - Cryo-EM structure determination
- QUANTIFICATION AND STATISTICAL ANALYSES
  - Statistical analysis

SUPPLEMENTAL INFORMATION

Supplemental information can be found online at https://doi.org/10.1016/j.immuni.2024.02.003.

ACKNOWLEDGMENTS

The authors thank A. Widge, M. Crank, J. Ledgerwood, L. Dropulic, and the VRC 200 study participants and study team for human samples; P. Wilson

(Cornell University) for providing 229-2G05 sequences; and R. Koup and members of the VRC Influenza Program for helpful discussion. This work was supported, in part, by the Vaccine Research Center, an intramural Division of NIAID, NIH; federal funds from the Frederick National Laboratory for Cancer Research, NIH, under contract HHSN261200800001 (to Y.T. and T.S.); and a generous gift from Open Philanthropy (to N.P.K.).

AUTHOR CONTRIBUTIONS

Conceptualization, J.L. and M.K.; formal analysis, J.L., Y.T., S.F.A., and M.K.; investigation, J.L., Y.T., L.N., J.E.R., A.C., T.S., R.A.G., H.Z.S., B.E.F., M.S., C.Y., A.J.S., R.R., S.F.A., N.P.K., and M.K.; resources, A.C. and M.S.; writing – original draft, J.L., Y.T., N.P.K., and M.K.; writing – review and editing, all authors; supervision, P.D.K., B.S.G., A.B.M., S.F.A., N.P.K., and M.K.; funding acquisition, P.D.K., B.S.G., A.B.M., and M.K.

DECLARATION OF INTERESTS

J.L., Y.T., S.F.A., and M.K. are named as inventors on patent applications filed by the National Institutes of Health, based on the studies presented in this paper. N.P.K. is a co-founder, shareholder, paid consultant, and chair of the scientific advisory board of Icosavax, Inc. The King lab has received unrelated sponsored research agreements from Pfizer and GSK.

Received: March 27, 2023
Revised: December 2, 2023
Accepted: February 6, 2024
Published: March 1, 2024

REFERENCES

1. Iuliano, A.D., Roguski, K.M., Chang, H.H., Muscatello, D.J., Palekar, R., Tempia, S., Cohen, C., Gran, J.M., Schanzer, D., Cowling, B.J., et al. (2018). Estimates of global seasonal influenza-associated respiratory mortality: a modelling study. Lancet *391*, 1285–1300.
2. Putri, W.C.W.S., Muscatello, D.J., Stockwell, M.S., and Newall, A.T. (2018). Economic burden of seasonal influenza in the United States. Vaccine *36*, 3960–3966.
3. Spreeuwenberg, P., Kroneman, M., and Paget, J. (2018). Reassessing the global mortality burden of the 1918 influenza pandemic. Am. J. Epidemiol. *187*, 2561–2567.
4. Chen, Y.-Q., Wohlbold, T.J., Zheng, N.-Y., Huang, M., Huang, Y., Neu, K.E., Lee, J., Wan, H., Rojas, K.T., Kirkpatrick, E., et al. (2018). Influenza infection in humans induces broadly cross-reactive and protective neuraminidase-reactive antibodies. Cell *173*, 417–429.e10.
5. Air, G.M., Laver, W.G., and Webster, R.G. (1987). Antigenic variation in influenza viruses. Contrib. Microbiol. Immunol. *8*, 20–59.
6. Wei, C.-J., Crank, M.C., Shiver, J., Graham, B.S., Mascola, J.R., and Nabel, G.J. (2020). Next-generation influenza vaccines: opportunities and challenges. Nat. Rev. Drug Discov. *19*, 239–252.
7. McMillan, C.L.D., Young, P.R., Watterson, D., and Chappell, K.J. (2021). The next generation of influenza vaccines: towards a universal solution. Vaccines (Basel) *9*, 26.
8. Kanekiyo, M., and Graham, B.S. (2021). Next-generation influenza vaccines. Cold Spring Harb. Perspect. Med. *11*, a038448.
9. Krammer, F., García-Sastre, A., and Palese, P. (2018). Is it possible to develop a "universal" influenza virus vaccine? Potential target antigens and critical aspects for a universal influenza vaccine. Cold Spring Harb. Perspect. Biol. *10*, a028845.
10. Krammer, F., Fouchier, R.A.M., Eichelberger, M.C., Webby, R.J., Shaw-Saliba, K., Wan, H., Wilson, P.C., Compans, R.W., Skountzou, I., and Monto, A.S. (2018). NAction! How Can Neuraminidase-Based Immunity Contribute to Better Influenza Virus Vaccines? mBio *9*. e02332–e02317.
11. McAuley, J.L., Gilbertson, B.P., Trifkovic, S., Brown, L.E., and McKimm-Breschkin, J.L. (2019). Influenza virus neuraminidase structure and functions. Front. Microbiol. *10*, 39.
12. Matrosovich, M.N., Matrosovich, T.Y., Gray, T., Roberts, N.A., and Klenk, H.D. (2004). Neuraminidase is important for the initiation of influenza virus infection in human airway epithelium. J. Virol. *78*, 12665–12667.
13. Madsen, A., Dai, Y.-N., McMahon, M., Schmitz, A.J., Turner, J.S., Tan, J., Lei, T., Alsoussi, W.B., Strohmeier, S., Amor, M., et al. (2020). Human antibodies targeting influenza B Virus neuraminidase active site are broadly protective. Immunity *53*, 852–863.e7.
14. Yasuhara, A., Yamayoshi, S., Kiso, M., Sakai-Tagawa, Y., Okuda, M., and Kawaoka, Y. (2022). A broadly protective human monoclonal antibody targeting the sialidase activity of influenza A and B virus neuraminidases. Nat. Commun. *13*, 6602.
15. Stadlbauer, D., Zhu, X., McMahon, M., Turner, J.S., Wohlbold, T.J., Schmitz, A.J., Strohmeier, S., Yu, W., Nachbagauer, R., Mudd, P.A., et al. (2019). Broadly protective human antibodies that target the active site of influenza virus neuraminidase. Science *366*, 499–504.
16. Cox, R.J. (2013). Correlates of protection to influenza virus, where do we go from here? Hum. Vaccin. Immunother. *9*, 405–408.
17. Memoli, M.J., Shaw, P.A., Han, A., Czajkowski, L., Reed, S., Athota, R., Bristol, T., Fargis, S., Risos, K., Powers, J.H., et al. (2016). Evaluation of antihemagglutinin and antineuraminidase antibodies as correlates of protection in an influenza A/H1N1 virus healthy human challenge model. mBio *7*, e00417–e00416.
18. Monto, A.S., Petrie, J.G., Cross, R.T., Johnson, E., Liu, M., Zhong, W., Levine, M., Katz, J.M., and Ohmit, S.E. (2015). Antibody to influenza virus neuraminidase: an independent correlate of protection. J. Infect. Dis. *212*, 1191–1199.
19. Couch, R.B., Atmar, R.L., Franco, L.M., Quarles, J.M., Wells, J., Arden, N., Niño, D., and Belmont, J.W. (2013). Antibody correlates and predictors of immunity to naturally occurring influenza in humans and the importance of antibody to the neuraminidase. J. Infect. Dis. *207*, 974–981.
20. Ng, S., Nachbagauer, R., Balmaseda, A., Stadlbauer, D., Ojeda, S., Patel, M., Rajabhathor, A., Lopez, R., Guglia, A.F., Sanchez, N., et al. (2019). Novel correlates of protection against pandemic H1N1 influenza A virus infection. Nat. Med. *25*, 962–967.
21. Wan, H., Yang, H., Shore, D.A., Garten, R.J., Couzens, L., Gao, J., Jiang, L., Carney, P.J., Villanueva, J., Stevens, J., et al. (2015). Structural characterization of a protective epitope spanning A(H1N1)pdm09 influenza virus neuraminidase monomers. Nat. Commun. *6*, 6114.
22. Gilchuk, I.M., Bangaru, S., Gilchuk, P., Irving, R.P., Kose, N., Bombardi, R.G., Thornburg, N.J., Creech, C.B., Edwards, K.M., Li, S., et al. (2019). Influenza H7N9 virus neuraminidase-specific human monoclonal antibodies inhibit viral egress and protect from lethal influenza infection in mice. Cell Host Microbe *26*, 715–728.e8.
23. Zhu, X., Turner, H.L., Lang, S., McBride, R., Bangaru, S., Gilchuk, I.M., Yu, W., Paulson, J.C., Crowe, J.E., Jr., Ward, A.B., et al. (2019). Structural basis of protection against H7N9 influenza virus by human anti-N9 neuraminidase antibodies. Cell Host Microbe *26*, 729–738.e4.
24. Saito, T., Taylor, G., Laver, W.G., Kawaoka, Y., and Webster, R.G. (1994). Antigenicity of the N8 influenza A virus neuraminidase: existence of an epitope at the subunit interface of the neuraminidase. J. Virol. *68*, 1790–1796.
25. Casalino, L., Seitz, C., Lederhofer, J., Tsybovsky, Y., Wilson, I.A., Kanekiyo, M., and Amaro, R.E. (2022). Breathing and tilting: mesoscale simulations illuminate influenza glycoprotein vulnerabilities. ACS Cent. Sci. *8*, 1646–1663.
26. Ke, Z., Oton, J., Qu, K., Cortese, M., Zila, V., McKeane, L., Nakane, T., Zivanov, J., Neufeldt, C.J., Cerikan, B., et al. (2020). Structures and distributions of SARS-CoV-2 spike proteins on intact virions. Nature *588*, 498–502.
27. Benton, D.J., Nans, A., Calder, L.J., Turner, J., Neu, U., Lin, Y.P., Ketelaars, E., Kallewaard, N.L., Corti, D., Lanzavecchia, A., et al. (2018). Influenza hemagglutinin membrane anchor. Proc. Natl. Acad. Sci. USA *115*, 10112–10117.

28. Wang, Z., Amaya, M., Addetia, A., Dang, H.V., Reggiano, G., Yan, L., Hickey, A.C., DiMaio, F., Broder, C.C., and Veesler, D. (2022). Architecture and antigenicity of the Nipah virus attachment glycoprotein. Science *375*, 1373–1378.

29. Ellis, D., Lederhofer, J., Acton, O.J., Tsybovsky, Y., Kephart, S., Yap, C., Gillespie, R.A., Creanga, A., Olshefsky, A., Stephens, T., et al. (2022). Structure-based design of stabilized recombinant influenza neuraminidase tetramers. Nat. Commun. *13*, 1825.

30. Burton, D.R. (2002). Antibodies, viruses and vaccines. Nat. Rev. Immunol. *2*, 706–713.

31. Rappuoli, R., Bottomley, M.J., D'Oro, U., Finco, O., and De Gregorio, E. (2016). Reverse vaccinology 2.0: human immunology instructs vaccine antigen design. J. Exp. Med. *213*, 469–481.

32. Webster, R.G., Brown, L.E., and Laver, W.G. (1984). Antigenic and biological characterization of influenza virus neuraminidase (N2) with monoclonal antibodies. Virology *135*, 30–42.

33. Jedrzejas, M.J., Singh, S., Brouillette, W.J., Laver, W.G., Air, G.M., and Luo, M. (1995). Structures of aromatic inhibitors of influenza virus neuraminidase. Biochemistry *34*, 3144–3151.

34. Kosik, I., Angeletti, D., Gibbs, J.S., Angel, M., Takeda, K., Kosikova, M., Nair, V., Hickman, H.D., Xie, H., Brooke, C.B., et al. (2019). Neuraminidase inhibition contributes to influenza A virus neutralization by anti-hemagglutinin stem antibodies. J. Exp. Med. *216*, 304–316.

35. Chen, Y.-Q., Lan, L.Y.-L., Huang, M., Henry, C., and Wilson, P.C. (2019). Hemagglutinin stalk-reactive antibodies interfere with influenza virus neuraminidase activity by steric hindrance. J. Virol. *93*. e01526–e01518.

36. Patel, M.C., Flanigan, D., Feng, C., Chesnokov, A., Nguyen, H.T., Elal, A.A., Steel, J., Kondor, R.J., Wentworth, D.E., Gubareva, L.V., et al. (2022). An optimized cell-based assay to assess influenza virus replication by measuring neuraminidase activity and its applications for virological surveillance. Antiviral Res. *208*, 105457.

37. Lambré, C.R., Terzidis, H., Greffard, A., and Webster, R.G. (1990). Measurement of anti-influenza neuraminidase antibody using a peroxidase-linked lectin and microtitre plates coated with natural substrates. J. Immunol. Methods *135*, 49–57.

38. Giurgea, L.T., Morens, D.M., Taubenberger, J.K., and Memoli, M.J. (2020). Influenza neuraminidase: A neglected protein and its potential for a better influenza vaccine. Vaccines (Basel) *8*, 409.

39. Creanga, A., Gillespie, R.A., Fisher, B.E., Andrews, S.F., Lederhofer, J., Yap, C., Hatch, L., Stephens, T., Tsybovsky, Y., Crank, M.C., et al. (2021). A comprehensive influenza reporter virus panel for high-throughput deep profiling of neutralizing antibodies. Nat. Commun. *12*, 1722.

40. Corti, D., Voss, J., Gamblin, S.J., Codoni, G., Macagno, A., Jarrossay, D., Vachieri, S.G., Pinna, D., Minola, A., Vanzetta, F., et al. (2011). A neutralizing antibody selected from plasma cells that binds to group 1 and group 2 influenza A hemagglutinins. Science *333*, 850–856.

41. Wu, Y., Gao, F., Qi, J., Bi, Y., Fu, L., Mohan, S., Chen, Y., Li, X., Pinto, B.M., Vavricka, C.J., et al. (2016). Resistance to mutant Group 2 influenza virus neuraminidases of an oseltamivir-zanamivir hybrid inhibitor. J. Virol. *90*, 10693–10700.

42. Momont, C., Dang, H.V., Zatta, F., Hauser, K., Wang, C., di Iulio, J., Minola, A., Czudnochowski, N., De Marco, A., Branch, K., et al. (2023). A pan-influenza antibody inhibiting neuraminidase via receptor mimicry. Nature *618*, 590–597.

43. Wohlbold, T.J., Podolsky, K.A., Chromikova, V., Kirkpatrick, E., Falconieri, V., Meade, P., Amanat, F., Tan, J., tenOever, B.R., Tan, G.S., et al. (2017). Broadly protective murine monoclonal antibodies against influenza B virus target highly conserved neuraminidase epitopes. Nat. Microbiol. *2*, 1415–1424.

44. Yuan, P., Thompson, T.B., Wurzburg, B.A., Paterson, R.G., Lamb, R.A., and Jardetzky, T.S. (2005). Structural studies of the parainfluenza virus 5 hemagglutinin-neuraminidase tetramer in complex with its receptor, sialyllactose. Structure *13*, 803–815.

45. Crennell, S., Takimoto, T., Portner, A., and Taylor, G. (2000). Crystal structure of the multifunctional paramyxovirus hemagglutinin-neuraminidase. Nat. Struct. Biol. *7*, 1068–1074.

46. Lawrence, M.C., Borg, N.A., Streltsov, V.A., Pilling, P.A., Epa, V.C., Varghese, J.N., McKimm-Breschkin, J.L., and Colman, P.M. (2004). Structure of the haemagglutinin-neuraminidase from human parainfluenza virus type III. J. Mol. Biol. *335*, 1343–1357.

47. Marcink, T.C., Zipursky, G., Cheng, W., Stearns, K., Stenglein, S., Golub, K., Cohen, F., Bovier, F., Pfalmer, D., Greninger, A.L., et al. (2023). Subnanometer structure of an enveloped virus fusion complex on viral surface reveals new entry mechanisms. Sci. Adv. *9*, eade2727.

48. Lei, R., Kim, W., Lv, H., Mou, Z., Scherm, M.J., Schmitz, A.J., Turner, J.S., Tan, T.J.C., Wang, Y., Ouyang, W.O., et al. (2023). Leveraging vaccination-induced protective antibodies to define conserved epitopes on influenza N2 neuraminidase. Immunity *56*, 2621–2634.e6.

49. Hansen, L., McMahon, M., Turner, H.L., Zhu, X., Turner, J.S., Ozorowski, G., Stadlbauer, D., Vahokoski, J., Schmitz, A.J., Rizk, A.A., et al. (2023). Human anti-N1 monoclonal antibodies elicited by pandemic H1N1 virus infection broadly inhibit HxN1 viruses in vitro and in vivo. Immunity *56*, 1927–1938.e8.

50. Zhou, T., Georgiev, I., Wu, X., Yang, Z.-Y., Dai, K., Finzi, A., Kwon, Y.D., Scheid, J.F., Shi, W., Xu, L., et al. (2010). Structural basis for broad and potent neutralization of HIV-1 by antibody VRC01. Science *329*, 811–817.

51. Scheres, S.H.W. (2012). RELION: implementation of a Bayesian approach to cryo-EM structure determination. J. Struct. Biol. *180*, 519–530.

52. Zheng, S.Q., Palovcak, E., Armache, J.P., Verba, K.A., Cheng, Y., and Agard, D.A. (2017). MotionCor2: anisotropic correction of beam-induced motion for improved cryo-electron microscopy. Nat. Methods *14*, 331–332.

53. Rohou, A., and Grigorieff, N. (2015). CTFFIND4: fast and accurate defocus estimation from electron micrographs. J. Struct. Biol. *192*, 216–221.

54. Wagner, T., Merino, F., Stabrin, M., Moriya, T., Antoni, C., Apelbaum, A., Hagel, P., Sitsel, O., Raisch, T., Prumbaum, D., et al. (2019). SPHIRE-crYOLO is a fast and accurate fully automated particle picker for cryo-EM. Commun. Biol. *2*, 218.

55. Kucukelbir, A., Sigworth, F.J., and Tagare, H.D. (2014). Quantifying the local resolution of cryo-EM density maps. Nat. Methods *11*, 63–65.

56. Sanchez-Garcia, R., Gomez-Blanco, J., Cuervo, A., Carazo, J.M., Sorzano, C.O.S., and Vargas, J. (2021). DeepEMhancer: a deep learning solution for cryo-EM volume post-processing. Commun. Biol. *4*, 874.

57. Waterhouse, A., Bertoni, M., Bienert, S., Studer, G., Tauriello, G., Gumienny, R., Heer, F.T., de Beer, T.A.P., Rempfer, C., Bordoli, L., et al. (2018). SWISS-MODEL: homology modelling of protein structures and complexes. Nucleic Acids Res. *46*, W296–W303.

58. Pettersen, E.F., Goddard, T.D., Huang, C.C., Couch, G.S., Greenblatt, D.M., Meng, E.C., and Ferrin, T.E. (2004). UCSF Chimera–a visualization system for exploratory research and analysis. J. Comput. Chem. *25*, 1605–1612.

59. Adams, P.D., Afonine, P.V., Bunkóczi, G., Chen, V.B., Davis, I.W., Echols, N., Headd, J.J., Hung, L.-W., Kapral, G.J., Grosse-Kunstleve, R.W., et al. (2010). PHENIX: a comprehensive Python-based system for macromolecular structure solution. Acta Crystallogr. D Biol. Crystallogr. *66*, 213–221.

60. Emsley, P., and Cowtan, K. (2004). Coot: model-building tools for molecular graphics. Acta Crystallogr. D Biol. Crystallogr. *60*, 2126–2132.

61. Davis, I.W., Murray, L.W., Richardson, J.S., and Richardson, D.C. (2004). MolProbity: structure validation and all-atom contact analysis for nucleic acids and their complexes. Nucleic Acids Res. *32*, W615–W619.

62. Krissinel, E., and Henrick, K. (2007). Inference of macromolecular assemblies from crystalline state. J. Mol. Biol. *372*, 774–797.

63. Sievers, F., Wilm, A., Dineen, D., Gibson, T.J., Karplus, K., Li, W., Lopez, R., McWilliam, H., Remmert, M., Söding, J., et al. (2011). Fast, scalable generation of high-quality protein multiple sequence alignments using Clustal Omega. Mol. Syst. Biol. *7*, 539.

64. Crooks, G.E., Hon, G., Chandonia, J.-M., and Brenner, S.E. (2004). WebLogo: a sequence logo generator. Genome Res *14*, 1188–1190.

65. Schneider, T.D., and Stephens, R.M. (1990). Seqeunce logos: a new way to display consensus sequences. Nucleic Acids Res *18*, 6097–6100.

66. Doria-Rose, N.A., Bhiman, J.N., Roark, R.S., Schramm, C.A., Gorman, J., Chuang, G.Y., Pancera, M., Cale, E.M., Ernandes, M.J., Louder, M.K., et al. (2016). New member of the V1V2-directed CAP256-VRC26 lineage that shows increased breadth and exceptional potency. J. Virol. *90*, 76–91.

67. Tiller, T., Meffre, E., Yurasov, S., Tsuiji, M., Nussenzweig, M.C., and Wardemann, H. (2008). Efficient generation of monoclonal antibodies from single human B cells by single cell RT-PCR and expression vector cloning. J. Immunol. Methods *329*, 112–124.

68. Wu, X., Yang, Z.-Y., Li, Y., Hogerkorp, C.-M., Schief, W.R., Seaman, M.S., Zhou, T., Schmidt, S.D., Wu, L., Xu, L., et al. (2010). Rational design of envelope identifies broadly neutralizing human monoclonal antibodies to HIV-1. Science *329*, 856–861.

69. Westgeest, K.B., de Graaf, M., Fourment, M., Bestebroer, T.M., van Beek, R., Spronken, M.I.J., de Jong, J.C., Rimmelzwaan, G.F., Russell, C.A., Osterhaus, A.D.M.E., et al. (2012). Genetic evolution of the neuraminidase of influenza A (H3N2) viruses from 1968 to 2009 and its correspondence to haemagglutinin evolution. J. Gen. Virol. *93*, 1996–2007.

70. Westgeest, K.B., Russell, C.A., Lin, X., Spronken, M.I.J., Bestebroer, T.M., Bahl, J., van Beek, R., Skepner, E., Halpin, R.A., de Jong, J.C., et al. (2014). Genomewide analysis of reassortment and evolution of human influenza A(H3N2) viruses circulating between 1968 and 2011. J. Virol. *88*, 2844–2857.

71. Varghese, J.N., Laver, W.G., and Colman, P.M. (1983). Structure of the influenza virus glycoprotein antigen neuraminidase at 2.9 A resolution. Nature *303*, 35–40.

72. Han, Y., Fan, X., Wang, H., Zhao, F., Tully, C.G., Kong, J., Yao, N., and Yan, N. (2020). High-yield monolayer graphene grids for near-atomic resolution cryoelectron microscopy. Proc. Natl. Acad. Sci. USA *117*, 1009–1014.

73. Henderson, R., Sali, A., Baker, M.L., Carragher, B., Devkota, B., Downing, K.H., Egelman, E.H., Feng, Z., Frank, J., Grigorieff, N., et al. (2012). Outcome of the first electron microscopy validation task force meeting. Structure *20*, 205–214.

74. Liebschner, D., Afonine, P.V., Baker, M.L., Bunkóczi, G., Chen, V.B., Croll, T.I., Hintze, B., Hung, L.W., Jain, S., McCoy, A.J., et al. (2019). Macromolecular structure determination using X-rays, neutrons and electrons: recent developments in Phenix. Acta Crystallogr. D Struct. Biol. *75*, 861–877.

75. Afonine, P.V., Klaholz, B.P., Moriarty, N.W., Poon, B.K., Sobolev, O.V., Terwilliger, T.C., Adams, P.D., and Urzhumtsev, A. (2018). New tools for the analysis and validation of cryo-EM maps and atomic models. Acta Crystallogr. D Struct. Biol. *74*, 814–840.

STAR★METHODS

KEY RESOURCES TABLE

REAGENT or RESOURCE	SOURCE	IDENTIFIER
Antibodies		
NDS.1	Produced in house (this study)	N/A
NDS.1.1	Produced in house (this study)	N/A
NDS.1.2	Produced in house (this study)	N/A
NDS.3	Produced in house (this study)	N/A
NDS.5	Produced in house (this study)	N/A
NDS.6	Produced in house (this study)	N/A
229-2G05	Produced in house; Chen et al.[4]	N/A
1G01	Produced in house; Stadlbauer et al.[15]	N/A
VRC01	Produced in house; Zhou et al.[50]	N/A
Fi6v3	Produced in house; Corti et al.[40]	N/A
BV510 Mouse Anti-Human CD3 (clone OKT3)	Biolegend	Cat# 317332; RRID: AB_2561943
BV510 Mouse Anti-Human CD14 (clone M5E2)	Biolegend	Cat# 301842; RRID: AB_2561946
BV510 Mouse Anti-Human CD56 (clone HCD56)	Biolegend	Cat# 318340; RRID: AB_2561944
BV421 Mouse Anti-Human CD19 (clone HIB19)	Biolegend	Cat# 302234; RRID: AB_11142678
APC/Fire 750 Mouse Anti-Human CD20 (clone 2H7)	Biolegend	Cat# 302357; RRID: AB_2572125
BV605 Mouse Anti-Human CD27 (clone O323)	Biolegend	Cat# 302830; RRID: AB_2561450
AF700 Mouse Anti-Human CD38 (clone HIT2)	Biolegend	Cat# 303524; RRID: AB_2072781
ECD Mouse Anti-Human CD19 (clone J3-119)	Beckman Coulter	Cat# IM2708U
PE-Cy5 Mouse Anti-Human CD21 (clone B-ly4)	BD Biosciences	Cat# 551064; RRID: AB_394028
PerCP-Cy5.5 Mouse Anti-Human IgM (clone G20-127)	BD Biosciences	Cat# 561285; RRID: AB_10611998
BV421 Mouse Anti-Human IgG (clone G18-145)	BD Biosciences	Cat# 562581; RRID: AB_2737665
BV750 Mouse Anti-Human IgG (clone G18-145)	BD Biosciences	Cat# 746959; RRID: AB_2871743
Goat Anti-Human IgG-HRP conjugated	Southern Biotech	Cat# 2040-05
Bacterial and Virus Strains		
replication-restricted reporter virus H3N2 A/Aichi/2/1968	Produced in house; Creanga et al.[39]	N/A
replication-restricted reporter virus H3N2 A/Philippines/2/1982	Produced in house; Creanga et al.[39]	N/A
replication-restricted reporter virus H3N2 A/Moscow/10/1999	Produced in house; Creanga et al.[39]	N/A
replication-restricted reporter virus H3N2 A/Wisconsin/67/2005	Produced in house; Creanga et al.[39]	N/A
replication-restricted reporter virus H3N2v A/Indiana/10/2011	Produced in house; Creanga et al.[39]	N/A
replication-restricted reporter virus H3N2 A/Switzerland/9715293/2013	Produced in house; Creanga et al.[39]	N/A
replication-restricted reporter virus H3N2 A/duck/France/161005/2016	Produced in house; Creanga et al.[39]	N/A
replication-restricted reporter virus H3N2 A/Darwin/106/2020	Produced in house; Creanga et al.[39]	N/A
replication-restricted reporter virus H3N2 A/Darwin/6/2021	Produced in house; Creanga et al.[39]	N/A
replication-restricted reporter virus H1N2 A/swine/Germany/Bak50/2017	Produced in house; Creanga et al.[39]	N/A
replication-restricted reporter virus H9N2 H9N2 A/Guangxi-Xiangshan/11522/2018	Produced in house; Creanga et al.[39]	N/A

(*Continued on next page*)

Continued

REAGENT or RESOURCE	SOURCE	IDENTIFIER
rewired replication-restricted reporter virus H2N2 A/Singapore/1/1957	Produced in house; Creanga et al.[39]	N/A
rewired replication-restricted reporter virus H2N2 A/Ann Arbor/7/1967	Produced in house; Creanga et al.[39]	N/A
H3N2 A/Philippines/2/1982	FDA	C6066
Biological Samples		
Human PBMCs	VRC	ClinicalTrials.gov identifier NCT00067054
Human serum and plasma	VRC	ClinicalTrials.gov identifier NCT00067054
Chemicals, Peptides, and Recombinant Proteins		
N2 WT A/Moscow/10/1999	Produced in house	N/A
N2 WT A/Wisconsin/67/2005	Produced in house	N/A
N2 WT A/Darwin/6/2021	Produced in house	N/A
N2 WT A/Indiana/10/2011	Produced in house	N/A
N2 A/Darwin/6/2021 T265N/K267T_V313N/R315T	Produced in house	N/A
N2 A/Darwin/6/2021 E119V_I222L	Produced in house	N/A
N1 sNAp A/WSN/1933	Produced in house; Ellis et al.[29]	N/A
N1 sNAp A/Vietnam/1203/2004	Produced in house; Ellis et al.[29]	N/A
N1 sNAp A/California/04/2009	Produced in house; Ellis et al.[29]	N/A
N1 sNAp A/Michigan/45/2015	Produced in house; Ellis et al.[29]	N/A
N8 sNAp A/Jiangxi-Donghu/346-2/2013	Produced in house; Ellis et al.[29]	N/A
N3 WT A/Swine/Missouri/2006	Produced in house; Ellis et al.[29]	N/A
NA WT B/Colorado/06/2017	Produced in house; Ellis et al.[29]	N/A
rProtein A Sepharose™ Fast Flow	Cytiva	Cat# 17-1279-03
IgG elution buffer	Pierce	Cat# 21009
ExpiFectamine™293 transfection kit	ThermoFisher Scientific	Cat# A14524
Ni-Sepharose excel resin	Cytiva	Cat# 17371201
Zanamivir	Sigma Aldrich	Cat# SML0492-50MG
Lectin from Arachis hypogaea (peanut)	Millipore Sigma	Cat# L7759
Phosphate-Citrate Buffer with Sodium Perborate	Millipore Sigma	Cat# P4922
Coating Solution Concentrate Kit	Seracare	Cat# 5150-0014
Fetuin	Millipore Sigma	Cat# F3385
o-Phenylenediamine dihydrochloride	Millpore Sigma	Cat# P8287
TPCK-Trypsin	Milllipore Sigma	Cat# T1426
Alexa Flour™ 647 Microscale Protein Labeling Kit	ThermoFisher Scientific	Cat# A30009
Alexa Fluor™ 488 Microscale Protein Labeling Kit	ThermoFisher Scientific	Cat# A30006
Critical Commercial Assays		
NA-Fluor™ Influenza Neuraminidase Assay Kit	ThermoFisher Scientific	Cat# 4457091
Deposited Data		
NDS.1 Fab–1G01 Fab–IN11v N2 NA cryo-EM structure	This study	EMD-29907; EMD-29908; PDB 8GAT; PDB 8GAU
NDS.3 Fab–DW21 N2 NA cryo-EM structure	This study	EMD-299909; PDB 8GAV
Experimental Models: Cell Lines		
Expi293 cells	Thermo Fisher Scientific	Cat#A14527
MDCK-SIAT1-PB1 cells	Produced in house; Creanga et al.[39]	N/A
MDCK-SIAT1	MilliporeSigma	SKU#05071502
Experimental Models: Organisms/Strains		
BALB/c	Envigo	BALB/cAnNHsd

(*Continued on next page*)

Continued

REAGENT or RESOURCE	SOURCE	IDENTIFIER
Software and Algorithms		
Flowjo v10	TreeStar	https://www.flowjo.com; RRID: SCR_008520
Prism v10.1.1	GraphPad	https://www.graphpad.com; RRID: SCR_002798
Octet Analysis v11	Sartorius	https://www.sartorius.com
Inkscape v1.2.2	Inkscape	https://inkscape.org
Biorender	Biorender	https://biorender.com
RELION 3	Scheres[51]	https://relion.readthedocs.io/en/release-5.0/
MotionCor2	Zheng et al.[52]	https://emcore.ucsf.edu/ucsf-software
ctffind4	Rohou and Grigorieff[53]	https://grigoriefflab.umassmed.edu/ctffind4
crYOLO	Wagner et al.[54]	https://cryolo.readthedocs.io/en/stable/
ResMap	Kucukelbir et al.[55]	https://resmap.sourceforge.net/
DeepEMhancer	Sanchez-Garcia et al.[56]	https://github.com/rsanchezgarc/deepEMhancer
SWISS-MODEL	Waterhouse et al.[57]	https://swissmodel.expasy.org/
UCSF Chimera	Pettersen et al.[58]	https://www.cgl.ucsf.edu/chimera/
Phenix	Adams et al.[59]	https://phenix-online.org/
Coot	Emsley et al.[60]	https://www2.mrc-lmb.cam.ac.uk/personal/pemsley/coot/
Molprobity	Davis et al.[61]	http://molprobity.biochem.duke.edu/
PDBe PISA	Krissinel et al.[62]	https://www.ebi.ac.uk/pdbe/pisa/
Clustal Omega	Sievers et al.[63]	https://www.ebi.ac.uk/jdispatcher/msa/clustalo
WebLogo v2.8.2	Crooks et al.[64]; Schneider and Stephens[65]	https://weblogo.berkeley.edu
Other		
Superdex 200 Increase 10/300GL	Cytiva	Cat# 28990944

RESOURCE AVAILABILITY

Lead contact

Further information and requests for resources and reagents should be directed to and will be fulfilled by the lead contact, Masaru Kanekiyo (kanekiyom@nih.gov).

Materials availability

All unique and stable materials generated in this study are available from the lead contact under a Material Transfer Agreement.

Data and code availability

The data that support the findings of this study are available from the corresponding author on request. Cryo-EM maps have been deposited in the Electron Microscopy Database under accession codes EMDB: EMD-29907, EMD-29908, and EMD-29909. Model coordinates habe been deposited in the Protein database under accession codes PDB: 8GAT, 8GAU, and 8GAV.

EXPERIMENTAL MODEL AND STUDY PARTICIPANT DETAILS

Human specimens

Human PBMC samples used in this study were obtained under the study, VRC 200, a protocol for apheresis and specimen collection procedures to obtain plasma, PBMCs and other specimens for research studies (ClinicalTrials.gov identifier NCT00067054) at the National Institutes of Health (NIH) Clinical Center by the Vaccine Research Center (VRC) Clinical Trials Program, National Institute of Allergy and Infectious Disease (NIAID), NIH in Bethesda, MD. The trial protocol was reviewed and approved by the NIAID

Institutional Review Board. Informed consent was obtained from every enrolled participant and conduct of the study complied with all relevant ethical regulations. Compensation was provided to participants for their time and effort related to participation in this clinical trial research study. PBMCs, serum (donor A) and plasma (donor B) samples were collected two to six weeks post-confirmed influenza positive PCR test for donor A and donor B. Donor A, male, born in 1956, sample collection in 2015; donor B, born 1997, sample collection in 2021; and donor 229-14-036,[4] female, age 46, sample collection on day 7 after confirmed influenza infection in 2014.

Mice

BALB/cAnNHsd female mice between 4-6 weeks of age were purchased from Envigo and were housed either in a conventional or specific pathogen free (SPF) animal facility on a 12-hour light/dark cycle under ambient conditions with free access to food and water. Animals were randomly assigned to experimental groups. All experiments were done in accordance with approved guidelines, regulations, and protocols as determined and approved by the Institutional Animal Care and Use Committee at Bioqual, Inc., Rockville, MD. The research facility is AAALAC International accredited and standards for all animal care (acquisition, breeding, and experimental protocols), biosafety, and personnel occupational health and safety conform to all Federal, State and local regulations.

METHOD DETAILS

Single-cell sorting, immunoglobulin amplification, sequencing and mAb production

Cryopreserved peripheral blood mononuclear cell (PBMC) samples were thawed and stained with monoclonal antibodies against human CD3 (BioLegend), CD14 (BioLegend), CD56 (BioLegend), CD19 (BioLegend or Beckam Coulter), CD20 (Biolegend), CD21 (BD), CD27 (BioLegend), CD38 (BioLegend), IgM (BD) and IgG (BD). The NA probes of N2 A/Wisconsin/67/2005 (WI05) or N2 A/Darwin/6/2021 (DW21) were conjugated with either AF488 or AF647 fluorochrome, respectively, according to the manufacturer's instruction (Microscale Protein Labeling Kit, Thermo Fisher Scientific) prior to use in flow cytometry. Non-B cells and dead cells were gated out with CD3, CD14, CD56 and Aqua (cell viability dye) staining. Memory B cells were gated on as $CD19^{+}$, $CD38^{low}$, IgM^{-} and IgG^{+} or IgG^{+} and $CD20^{+}$. NA-binding memory B cells were single-cell sorted into 96-well plates (Bio-Rad) using an FACS Aria Instrument (BD). Plates were subjected to reverse transcription PCR and cDNA were used for PCR to amplify immunoglobulin (Ig) heavy and light chain genes as described previously.[66,67] PCR products were sequenced by Sanger sequencing, and sequences were analyzed with the IMGT V-Quest (imgt.org/IMGT_vquest). Paired Ig heavy and light chain sequences were synthesized and subcloned into IgG1 heavy chain and kappa or lambda light chain backbone expression vectors, respectively (GenScript). Antibodies were expressed recombinantly by transient transfection of Ig expression plasmids in Expi293 cells (ThermoFisher Scientific) with ExpiFectamine™293 Transfection Kit (ThermoFisher Scientific). Supernatant was harvested 5 days post transfection and antibody was purified by using Protein A Sepharose (Cytiva). Control antibodies were generated as described above. 1G01,[15] a broadly reactive anti-NA mAb, and VRC01, an irrelevant mAb that binds to HIV-1 Env,[50,68] were used as positive and negative control, respectively in assays throughout the study.

Cell lines

Expi293 cells, purchased from Thermo Fisher Scientific (Catalog A14527), were cultured in Expi293 Expression Medium (Life Technologies) at 37°C with 8% CO_2 and agitating at 120 rpm. MDCK-SIAT1-PB1 cells used for virus propagation, growth inhibition assay, and NAI by MUNANA assay were described previously.[39] MDCK-SIAT1-PB1 cells were maintained in DMEM supplemented with 10% FBS, geneticin (1 mg ml^{-1}) and puromycin (0.25 μg ml^{-1}) at 37°C with 5% CO_2.

Viruses

Rescue and propagation of replication-restricted reporter (R3) influenza viruses used in this study was described previously.[39] Briefly, H3N2 viruses (A/Aichi/2/1968, A/Philippines/2/1982, A/Moscow/10/1999, A/Wisconsin/67/2005, A/Indiana/10/2011, A/Switzerland/9715293/2013, A/duck/France/161005/2016, A/Darwin/106/2020, and A/Darwin/6/2021), H1N2 A/swine/Germany/Bak50/2017, and H9N2 A/Guangxi-Xiangshan/11522/2018 viruses used in this study are R3 viruses in which PB1 segment was modified to encode a fluorescent reporter, whereas A/Singapore/1/1957 H2N2 and A/Ann Arbor/7/1967 H2N2 viruses are rewired R3 (i.e., R4) in which HA coding region is inserted between PB1 segment genome packaging signals and the fluorescent reporter is inserted between HA segment genome packaging signals.[39]

Protein expression and purification

Recombinant NA proteins were expressed and purified as described previously.[29] Briefly, NA constructs were expressed by transient transfection in Expi293 cells (ThermoFisher Scientific) using the ExpiFectamine™293 Transfection Kit (ThermoFisher Scientific). Cell culture supernatants were harvested 5 days post-transfection, cleared, and filtered. Proteins were purified from clarified supernatants by immobilized metal affinity chromatography (IMAC) using Ni-Sepharose High-Performance resin (Cytiva). After incubating for 2 h at room temperature, bound proteins were eluted using an elution buffer (50 mM Tris-HCl, 0.5 M NaCl, 300 mM imidazole, pH 8). Proteins were further purified by size exclusion chromatography (SEC) into phosphate-buffer saline (PBS) using a Superdex 200 Increase 10/300 column (Cytiva).

NA sequence analysis

NA sequences comprising the entire coding region were retrieved from GISAID (gisaid.org) and aligned with the MUSCLE algorithm as implemented in Bioedit v7.2.5. To identify genetically representative NA sequences of seasonal H3N2 viruses, we used phylogenetic analyses described Westgeest et al.[69,70] for viruses circulating from 1968 to 2011 and the phylogenetic analysis described at nextstrain.org/flu/seasonal/h3n2/na/12y for viruses circulating between 2011 and 2022. A set of 188 non-redundant sequences of circulating human H3N2 viruses between 1968 and 2022 was used to generate the WebLogo (seasonal H3N2), whereas 25 representative sequences of human H3N2 along with 55 sequences of representative animal HxN2 viruses causing sporadic outbreaks in humans (e.g., H1N2, H3N2v, H9N2) were used to generate the WebLogo for HxN2 in Figure 4E. NA sequences used in the analyses were listed in Item S1. WebLogo plots were made by using the WebLogo v2.8.2 (weblogo.berkeley.edu) and manually curated in Inkscape (v1.2). We followed the N2 numbering scheme based on the A/Tokyo/3/1967.[71]

Enzyme-linked immunosorbent assay (ELISA)

MaxiSorp™ ELISA plates (Nunc) were coated with 2 μg ml^{-1} of recombinant NA protein and incubated overnight at 4°C. Plates were washed with PBS and 0.1% Tween 20 (PBS-T) and blocked with 5% skim milk in PBS at 37°C for 1 h. MAbs were diluted to 0.1 mg ml^{-1} and serially diluted threefold and added to the plates for 30 min at 37°C. After washing, HRP-conjugated secondary antibody (anti-human; Southern Biotech) was added and incubated for another 30 min at 37°C. Plates were developed with KPL TMB substrate and the reaction was stopped by the addition of 0.5 M H_2SO_4. Absorbance was measured at 450 nm (Biotek Neo2 plate reader).

For human convalescent samples, ELISA plates were coated with recombinant NA proteins and blocked as described above. Human serum and plasma samples were diluted to 1/25 and serially diluted in two-fold before added to the NA-coated ELISA plates. Plates were incubated for 1 h at 37°C followed by washing, secondary antibody, and development steps as described above.

Biolayer Interferometry (BLI)

BLI experiments were performed by using the Octet HTX instrument (Sartorius). HIS1K biosensors (Sartorius) were hydrated in PBS prior to use. Recombinant N2 NA proteins derived from A/Moscow/10/1999, A/Wisconsin/67/2005, A/Indiana/10/2011 and A/Darwin/6/2021 were immobilized on hydrated HIS1K biosensors through their hexahistidine tag at their N-termini. After brief (60 s) equilibration in assay buffer (25 mM Tris, 150 mM NaCl, 1% BSA, pH 8.0) the biosensors were dipped into a two-fold dilution series of NDS.1, NDS.1.1 or NDS.3 Fabs for 300 s. Starting concentration of Fabs was 400–800 nM. Biosensors were then dipped in the assay buffer to allow Fabs to dissociate from NA for 600 s. All assay steps were performed at 30°C with agitation set at 1,000 rpm. Baseline correction was carried out by subtracting the measurements recorded for a sensor loaded with the corresponding NA in the same buffer with no Fab. Data analysis and curve fitting were done with the Octet analysis software (version 12). Experimental data were fitted with the binding equations describing a 1:1 (Langmuir model) interaction.

Influenza replication inhibition neuraminidase-based assay (IRINA)

The viruses were diluted in Opti-MEM (Gibco) and 45 μl of titrated virus was added to 45 μl of Opti-MEM into a 96-well plate and incubated for 1 h at 37°C. MCDK-SIAT1-PB1 cells were trypsinized, washed once with PBS and resuspended in Opti-MEM. Thirty μl of MDCK-SIAT1-PB1 cells at a concentration of 1 × 10^6 cells ml^{-1} were added to each well containing the diluted virus. Twenty-five μl of virus-cell mixture was added to each 384 well in quadruplicate and incubated for 20–24 h at 37°C with 5% CO_2. Next day, mAbs were diluted in the assay buffer (NA-Fluor Influenza Neuraminidase Assay Kit; Thermo Fisher Scientific) at a starting concentration of 50 μg ml^{-1}. Culture supernatant of the 384-well plate was discarded and replenished with 25 μl diluted mAbs in quadruplicate. The plates were incubated for 1 h at 37°C with 5% CO_2, and 25 μL of assay substrate (NA-Fluor Influenza Neuraminidase Assay Kit; Thermo Fisher Scientific) was added to each well and incubated for another 1 h at 37°C with 5% CO_2. Reaction was then stopped by adding 50 μl of stop solution (NA-Fluor Influenza Neuraminidase Assay Kit; Thermo Fisher Scientific), and the plates were read using an excitation wavelength range of 350 nm to 365 nm and an emission wavelength range of 440 nm to 460 nm. Control wells without the virus infection were used for background subtraction.

Enzyme-linked lectin assay (ELLA)

MaxiSorp ELISA plates were coated with fetuin at 2.5 μg well^{-1} in the coating buffer (KPL coating solution; SeraCare), sealed and stored at 4°C overnight or until further use. Next day, the plates were washed with PBS-T. A two-fold serial dilution of virus was prepared in a separate 96-well plate with a starting dilution of 1:10 in sample diluent (PBS, 1% BSA, 0.5% Tween-20). Fifty μl of each virus dilution was added to the washed plate, sealed and incubated for 2 h at 37°C. The plates were washed six times with PBS-T, and 100 μl well^{-1} of HRP-conjugated peanut agglutinin (Sigma) at a concentration of 1 μg ml^{-1} was added to each plate. The plates were incubated for 2 h at room temperature and washed three times with PBS-T. The plates were developed with 100 μl well^{-1} SigmaFast OPD in the dark at room temperature and the reaction was stopped after 10 min with 100 μl well^{-1} of 0.5 M H_2SO_4. The plates were read at a wavelength of 490 nm (Biotek Neo2 plate reader).

For the neuraminidase inhibition assay, the plates were coated as described above. In a separate plate mAbs were diluted to a starting concentration of 50 μg ml^{-1}, serially two-fold diluted in sample diluent. Fifty μl well^{-1} of diluted virus was added to the fetuin-coated plate, and 50 μl well^{-1} of diluted mAb was added on top. Fifty μl well^{-1} of sample diluent was added on diluted virus for positive control wells, whereas 100 μL of sample diluent (without virus solution) was added for negative control wells. Plates

were sealed, gently mixed by tapping sides of plates, and incubated for 2 h at 37°C. The plates were washed, developed, and read as described above.

Virus Inhibition assay

MAbs were serially diluted three-fold at a starting concentration of 50 μg ml^{-1} in Opti-MEM, and the viruses were diluted in Opti-MEM supplemented with TPCK-treated trypsin (2 μg ml^{-1}). Forty-five μl of diluted mAb was incubated with 45 μl of diluted virus for 1 h at 37°C with 5% CO_2 in 96-well plates. MCDK-SIAT1-PB1 cells were trypsinized, washed once with PBS and resuspended in Opti-MEM. Thirty μl of MDCK-SIAT1-PB1 cells at a concentration of 1 × 10^6 cells ml^{-1} were added to each well containing mAb-virus mixture. Twenty-five μl of each cell-mAb-virus mixture was added in quadruplicate to 384-well plates, and the plates were incubated for 4–5 h at 37°C with 5% CO_2. After incubation, supernatant was removed and replenished with 25 μl of diluted mAb and 25 μl of Opti-MEM supplemented with TPCK-treated trypsin. Plates were incubated for 28–48 h at 37°C with 5% CO_2, and fluorescent cells (*i.e.*, reporter virus-infected cells) were detected with Celigo instrument (PerkinElmer). Results were analyzed and IC_{50} values were calculated with GraphPad Prism. Wells with zanamivir and without mAb were used as positive (100%) and negative (0%) controls for virus inhibition, respectively.

Passive transfer

For prophylactic treatment setting, six- to eight-week old female BALB/cJ mice (n = 9–10) were given 200 μl of mAbs solution at a concentration of 10, 3, or 1 mg kg^{-1} intraperitoneally 24 h prior to challenge. Mice were anesthetized and challenged intranasally with 10 × LD_{50} of H3N2 A/Philippines/2/1982 virus. For post-exposure treatment setting, mice (n = 9–10) were challenged with 5 × LD_{50} of H3N2 A/Philippines/2/1982 virus and treated 48 h later with 10 mg/kg of mAbs intraperitoneally. Body weight loss and clinical symptoms were monitored daily for 14 days post-infection and the humane endpoint was defined as a loss of 20% of the initial day 0 body weight.

Cryo-EM structure determination

Neuraminidase was mixed with the Fab fragments at a molar ratio of 1.5 Fab to 1 NA monomer. Quantifoil R 2/2 gold grids were glow-discharged using a PELCO easiGlow glow-discharger (air pressure: 0.39 mBar, current: 20 mA, duration: 30 s) immediately before use. Vitrification was performed at a total protein concentration of 0.15 mg/ml using a Thermo Scientific Vitrobot Mark IV plunger with the following parameters: chamber temperature of 4°C, chamber humidity of 95% and drop volume of 2.7 μl.

Datasets were collected on an FEI Titan Krios G1 electron microscope equipped with a Gatan K2 Summit direct electron detector operated in the counting mode. A single dataset, collected without tilting the stage, was used to determine the structure of the NDS.3–DW21 NA complex, which showed uniform particle distribution in the vitrified ice. In contrast, the NDS.1–IN11v NA complex demonstrated a strong preferred orientation, with only top views present in the initial dataset. To improve the angular distribution of the particles, Fab 1G01, which binds to the opposite side of the NA tetramer, was added to the NDS.1–IN11v NA complex before freezing, and datasets were collected and 0° and 30° of stage tilt. An additional dataset was recorded with the ternary complex prepared using Quantifoil R 2/2 gold grids covered with a monolayer of graphene oxide; these grids were produced in-house by following a published protocol.[72] The total protein concentration was reduced to 0.03 mg ml^{-1} for vitrification using graphene oxide-covered grids. All the above datasets were combined to obtain the structure of the NDS.1–1G01–IN11v NA complex.

The RELION 3.1 pipeline was used for single particle analysis,[51] with patch-based movie frame alignment performed with MotionCor2[52] and contrast transfer function (CTF) parameters determined using ctffind4.[53] Templates for automatic particle selection were obtained by 2D classification of particles picked from a small subset of micrographs using the template-free Laplacian-Gaussian filter-based approach. In the case of the NDS.1–1G01–IN11v NA complex, particles picked using the template-based approach in RELION were combined with particles selected using neural network-based picking with crYOLO,[54] followed by elimination of duplicates. Subsequent steps included rounds of 2D classification, initial 3D volume generation using the stochastic gradient descent algorithm, 3D classification, 3D auto-refinement, particle polishing and CTF refinement. In the case of the NDS.1–1G01–IN11v NA complex, the occupancy of NDS.1 Fab in the consensus map was incomplete. Therefore, we performed symmetry expansion followed by signal subtraction to isolate a single NA monomer with bound Fabs. This was followed by 3D classification without particle re-alignment to select complexes with occupied NDS.1 Fab. The resulting subset of particles was then subjected to 3D refinement with limited angular search. Resolutions were calculated using the gold-standard approach[73] at the Fourier shell correlation (FSC) curve threshold of 0.143. ResMap 1.1.4 was used to evaluate local resolution.[55] 3D map post-processing was performed using the standard automated approach implemented in RELION as well as with DeepEMhancer.[56]

To obtain the atomic models of the complexes, the SWISS-MODEL server[57] was used to generate homology models of NA and Fab molecules, which were then docked into the cryo-EM density using UCSF Chimera.[58] The atomic models were refined by alternating rounds of real-space refinement in Phenix[74] and model building in Coot.[60] Molprobity was used for structure validation.[60,61] Cryo-EM map-molecular model FSC curves were obtained with phenix.mtriage[75] at a threshold level of 0.5. NA–Fab interfaces were determined with PDBe PISA.[62] Clustal Omega was used for protein sequence alignment.[63]

QUANTIFICATION AND STATISTICAL ANALYSES

Statistical analysis

All *in vitro* experimental data shown except for B cell sorting and cryo-EM structure determination were representative of at least two independent experiments. Conclusions from the repeated experiments that are not shown in the manuscript are the same as those from the shown experiments. The sample size in *in vivo* experiments was determined based on the expected heterogeneity of the samples, the significance threshold (chosen at 0.05), the expected or observed difference, as well as previous publications and our pilot studies. The chosen sample size in each experiment is sufficient to generate statistically significant results. In all experiments, unless otherwise indicated, data are shown as mean with all data points or group mean ± SD, and statistical analyses were performed using GraphPad Prism (v9). Mantel-Cox test was used to compare Kaplan-Meier curves with Bonferroni correction applied. P values less than or equal to 0.05 (0.0033 after Bonferroni correction) were considered significant.